Abstract

We have implemented a new high-order low-order (HOLO) algorithm for solving thermal radiative transfer problems. The low-order (LO) system is based on spatial and angular moments of the transport equation and a linear-discontinuous finite-element spatial representation, producing equations similar to the standard S_2 equations. The LO solver is fully implicit in time and efficiently resolves the non-linear temperature dependence at each time step. The HO solver utilizes exponentially-convergent Monte Carlo (ECMC) to give a globally accurate solution for the angular intensity to a fixed-source, pure absorber transport problem. This global solution is used to compute consistency terms, which require the HO and LO solutions to converge towards the same solution. The use of ECMC allows for the efficient reduction of statistical noise in the MC solution, reducing inaccuracies introduced through the LO consistency terms. We compare results with an implicit Monte Carlo (IMC) code for one-dimensional, gray test problems and demonstrate the efficiency of ECMC over standard Monte Carlo in this HOLO algorithm.

Key Words: hybrid Monte Carlo, residual Monte Carlo, thermal radiative transfer

0.1 INTRODUCTION

We have implemented a high-order low-order (HOLO) algorithm for the case of 1D gray thermal radiative transfer (TRT) problems. The governing equations are the radiation and material energy balance equations, i.e.,

$$\frac{1}{c}\frac{\partial I(x,\mu,t)}{\partial t} + \mu\frac{\partial I(x,\mu,t)}{\partial x} + \sigma_t I(x,\mu,t) = \frac{\sigma_s}{2}\phi(x,t) + \frac{1}{2}\sigma_a acT^4(x,t) \quad (1)$$

$$\rho c_v \frac{\partial T(x,t)}{\partial t} = \sigma_a \phi(x,t) - \sigma_a acT^4(x,t). \quad (2)$$

In the above equations x is the position, t is the time, μ is the x-direction cosine of the angular intensity $I(x,\mu,t)$, and a, c, ρ, and c_v are the radiation constant, speed of light, mass density, and specific heat; σ_a, σ_s, and σ_t are the absorption, scattering, and total cross sections (cm^{-1}), respectively. The desired unknowns are the material temperature $T(x,t)$ and the scalar radiation intensity $\phi(x,t) = \int_{-1}^{1} I(x,\mu,t)d\mu$. The scalar intensity is related to the radiation energy density E by the relation $E = \phi/c$. The equations are strongly coupled through the gray Planckian emission source $\sigma_a acT^4$, which is a nonlinear function of temperature, and the absorption term $\sigma_a \phi$. In general, the material properties are a function of T. The temperature dependent material properties and absorption and reemission physics lead to systems that require solution in a mix of streaming and optically thick, diffusive regions.

Monte Carlo (MC) solution to the TRT equations is typically achieved by the implicit Monte Carlo (IMC) method [?]. This method partially linearizes Eq. (5) & Eq. (6) over a discrete time step, with material properties evaluated at the previous temperature. Linearization of the system produces a transport equation that contains an approximate emission source and an effective scattering cross section representing absorption and reemission of photons over a time step. This transport equation is advanced over a time step via MC. The MC simulation tallies energy absorption over a discretized spatial mesh. The energy absorption in each mesh cell is used to directly estimate a new end of time step temperature in that cell. In optically thick regions, or for large time steps, the effective scattering dominates interactions. In these diffusive regions IMC becomes computationally expensive. Acceleration methods typically attempt to improve efficiency by allowing particles to take discrete steps through optically thick regions based on a discretized diffusion approximation [?, ?]. In IMC the approximate linearization of the

emission source is not iterated on within a time step due to the large computational cost of the MC transport each time step; this imposes a limit on the time step size to produce physically accurate results [**?**].

In IMC the material and radiation energy fields are discretized spatially to solve for cell-averaged values. Inaccurate spatial representation of the emission source over a cell can result in energy propagating through the domain artificially fast, yielding non-physical results referred to as "teleportation error" [**?**]. The IMC method uses a fixup known as source tilting to mitigate this problem. Source tilting reconstructs a more accurate linear-discontinuous representation of the emission source within a cell based on the cell-averaged material temperatures in adjacent cells.

Moment-based hybrid Monte Carlo (MC) methods provide an alternative solution method. Recent work has focused on so-called high-order low-order (HOLO) approaches [**?**, **?**, **?**, **?**]. Such methods utilize a low-order (LO) operator based on angular moments of the transport equation, formulated over a fixed spatial mesh. Physics operators that are time consuming for MC to resolve, e.g., absorption-reemission and physical scattering events, are moved to the LO system. Newton methods allow for non-linearities in the LO equations to be fully resolved efficiently [**?**]. The high-order (HO) transport equation is defined by Eq. (5), with sources that are truly implicit in time estimated from the LO solution. The HO equation is solved via MC to produce a high-fidelity solution for the angular intensity. The MC estimate of the angular intensity is used to estimate consistency terms, present in the LO equations, that require the LO system to preserve the angular accuracy of the MC solution. The HO system does not directly estimate a new material temperature, eliminating stability issues that require linearization of the emission source.

Sufficient MC histories must be performed to eliminate statistical noise in the consistency terms that can contaminate the LO solution. Exponentially-convergent Monte Carlo (ECMC)[**?**, **?**] provides an algorithm that can efficiently reduce statistical noise to the same order as the HOLO iteration error with significantly less particle histories than standard MC. In particular, ECMC is exceptionally efficient in time-dependent TRT problems because information about the intensity from the previous time step can be used as an accurate initial guess for the new end of time step intensity. Additionally, no particle histories are required in regions where the radiation and material energy field are in equilibrium, similar to [**?**]. However, implementation of ECMC is non-trivial, requiring a finite-element representation of

the solution in all phase-space variables that are being sampled with MC. The fundamental transport of particles is the same as standard Monte Carlo transport codes, but the source will now contain positive and negative weight particles.

Our ECMC solver contains similarities to the residual Monte Carlo (RMC) HO solver in [?], with some key differences. The RMC algorithm uses a particular, fixed estimate of the solution to significantly reduce the statistical noise in the simulation compared to a standard MC simulation. The guess for the solution is chosen to produce only sources on the faces of cells, reducing the dimension of the phase-space to be sampled [?]. The RMC algorithm uses a piecewise constant trial space representation for the intensity in x and μ. The primary difference between the methods is that ECMC iteratively estimates the solution, in batches, producing a known MC estimate of the error in that estimate. The ECMC algorithm projects the intensity onto a linear-discontinuous finite-element (LDFE) trial space, although the RMC algorithm could similarly be formulated with an LDFE representation. Adaptive mesh-refinement can be used in ECMC to produce highly accurate solutions with minimal statistical noise, as long as sufficient particle histories are performed. The formulation of the residual in [?] use an estimate of the solution such that only face sources need to be sampled. This residual formulation can produce minimal statistical noise in slowly varying problems where the behavior of the system is near equilibrium. Our ECMC algorithm has similar statistical efficiency by choosing the previous time step intensity as the initial guess to the algorithm; however, a linear volumetric source must be sampled in addition to face sources. The ECMC algorithm will generally be more efficient in cases where the solution varies greatly over a time step or when very low statistical noise is desired. Generally, the minimum number of histories per batch to obtain convergence with the LDFE trial space is larger than a piece-wise constant representation because additional histories are needed to sufficiently estimate the first moment in x and μ of the intensity. It is noted that our formulation of the LO equations and consistency terms contrast greatly from the typical formulation in [?, ?, ?].

In this work, we demonstrate the utility of an S_2-like LO operator [?] in conjunction with an ECMC method [?] for the HO solver. The ECMC algorithm uses information about the intensity from the previous time step to reduce statistical noise to the same order as the HOLO iteration error with significantly less particle histories than standard MC simulations, with less computational cost than IMC per history. We have derived the LO operator

3

directly from the transport equation, using a linear-discontinuous (LD) finite-element (FE) spatial discretization for the HO and LO solutions. Herein we describe the algorithm and present results for 1D, gray test problems.

0.2 Overview of the HOLO Algorithm

For simplicity, our HOLO method will use a backwards Euler discretization in time, as well as constant specific heats and cell-wise constant cross sections. The time-discretized equations are

$$\mu\frac{\partial I^{n+1}}{\partial x} + \left(\sigma_t^{n+1} + \frac{1}{c\Delta t}\right)I^{n+1} = \frac{\sigma_s}{2}\phi^{n+1} + \frac{1}{2}\left(\sigma_a acT^4\right)^{n+1} + \frac{I^n}{c\Delta t} \qquad (3)$$

$$\rho c_v \frac{T^{n+1} - T^n}{\Delta t} = \sigma_a^{n+1}\phi^{n+1} - \sigma_a ac(T^4)^{n+1}, \qquad (4)$$

where Δt is the uniform time step size, the superscript n is used to indicate the n-th time step. Cross sections are evaluated at the end of time step temperature, i.e., $\sigma_a^{n+1} \equiv \sigma_a(T^{n+1})$. It is noted that in IMC the time derivative in Eq. (5) is typically treated continuously using time-dependent MC over each time step. Our HO transport equation is discrete in time for simpler application of ECMC and to avoid difficulties in coupling to the fully-discrete LO solver. However, this does introduce some artificial propagation of energy due to the implicit time differencing in optically thin regions.

In the HOLO context, the LO solver models isotropic scattering and resolves the material temperature spatial distribution $T(x)$ at each time step. The LO equations are formed via half-range angular and spatial moments of Eq. (7) and Eq. (8), formed over a spatial finite element mesh. The angular treatment in the LO equations has the same form as those used in the hybrid-S$_2$ method in [?], with element-averaged consistency parameters that are analogous to a variable Eddington factor. If the angular consistency parameters were exact, then the LO equations are exact, neglecting spatial discretization errors. These consistency parameters are lagged in each LO solve, estimated from the previous HO solution for $I^{n+1}(x,\mu)$, as explained below. For the initial LO solve for each time step, the parameters are calculated with $I^n(x,\mu)$. The discrete LO equations always conserve total energy, independent of the accuracy of the consistency terms. The LO system uses a LDFE spatial discretization for the temperature and half-range scalar intensities. The LDFE spatial discretization should correctly preserve

4

the equilibrium diffusion limit, a critical aspect for TRT equations [**?**, **?**]. Additionally, the implicit time discretization with sufficient convergence of the nonlinear emission source will ensure that the method will not exhibit maximum principle violations [**?**].

The solution to the LO system is used to construct a LDFE spatial representation of the isotropic scattering and emission sources on the right hand side of Eq. (7). The LDFE representation of the emission source mitigates teleportation error. This defines a fixed-source, pure absorber transport problem for the HO operator. This HO transport problem represents a characteristic method that uses MC to invert the continuous streaming plus removal operator with an LDFE representation of sources; the representation of sources is similar to the linear moments method discussed in [**?**]. We will solve this transport problem using ECMC. The output from ECMC is $\tilde{I}^{n+1}(x, \mu)$, a space-angle LDFE projection of the exact solution $I^{n+1}(x, \mu)$ to the described transport problem. Once computed, $\tilde{I}^{n+1}(x, \mu)$ is used to directly evaluate the necessary consistency parameters for the next LO solve. Since there is a global, functional representation of the angular intensity, LO parameters are estimated using quadrature and do not require additional tallies. The HO solution is not used to directly estimate a new temperature at the end of the time step; it is only used to estimate the angular consistency parameters for the LO equations, which eliminates typical operator splitting stability issues that require linearization of the emission source.

The process of performing subsequential HO and LO solves, within a single time step, can be repeated to obtain an increasingly accurate solution for $\phi^{n+1}(x)$ and $T^{n+1}(x)$. Thus, the HOLO algorithm, for the n-th time step, is

1. Perform a LO solve to produce an initial guess for $T^{n+1,0}(x)$ and $\phi^{n+1,0}(x)$, based on consistency terms estimated with $\tilde{I}^n$.

2. Solve the HO system for $\tilde{I}^{n+1,k+1/2}(x, \mu)$ with ECMC, based on the current LO estimate of the emission and scattering sources.

3. Compute LO consistency parameters with $\tilde{I}^{n+1,k+1/2}$.

4. Solve the LO system with HO consistency parameters to produce a new estimate of $\phi^{n+1,k+1}$ and $T^{n+1,k+1}$.

5. Optionally repeat $2-4$ until desired convergence is achieved.

6. Store $\tilde{I}^n \leftarrow \tilde{I}^{n+1}$, and move to the next time step.

where the superscript k denotes the outer HOLO iteration. The consistency terms force the HO and LO solutions for $\phi^{n+1}(x)$ to be consistent to the order of the current HOLO iteration error, as long as the LDFE spatial representation can accurately represent $\phi(x)$ and $T(x)$.

0.3 Overview

This document describes dissertation research over a new Monte Carlo algorithm for solution of thermal radiative transfer problems. Herein, a brief description of thermal radiative transfer and the model problem are given, followed by a discussion of the standard Monte Carlo solution method and other related research. An overview of the methodology and results performed thus far are given in Sec. 0.5. Then, the remaining topics for completing this dissertation research are discussed in Sec. 0.6. Finally, Sec. 0.7 provides a specific outline of the remaining research to be investigated and computational results to be generated.

0.4 Introduction

0.4.1 Thermal radiative transfer background

Thermal radiative transfer (TRT) physics describe the time-dependent energy distributions of a photon radiation field and a high-temperature material. The material and radiation exchange energy through absorption and emission of photons by the material. Accurate modeling of TRT physics becomes relevant in the high-energy, high-density physics regime. Typical computational applications of TRT include simulation of inertial confinement fusion and astrophysics phenomena. The transport of photons through a material is characterized by particle position, direction, and frequency. The material energy distribution is described by the material internal energy (often described by material temperature) as a function of position. The high-dimensional space results in a difficult, nonlinear transport problem.

This research will focus on a simplified 1D slab-geometry and frequency-integrated (grey) TRT model. The governing equations for this simplified

model are the radiation and material energy balance equations

$$\frac{1}{c}\frac{\partial I(x,\mu,t)}{\partial t} + \mu\frac{\partial I(x,\mu,t)}{\partial x} + \sigma_t I(x,\mu,t) = \frac{\sigma_s}{2}\phi(x,t) + \frac{1}{2}\sigma_a ac T^4(x,t) \quad (5)$$

$$\rho c_v \frac{\partial T(x,t)}{\partial t} = \sigma_a \phi(x,t) - \sigma_a ac T^4(x,t). \quad (6)$$

In the above equations the fundamental unknowns are the material temperature $T(x,t)$ and the angular intensity $I(x,\mu,t)$ of radiation, where x is the position, t is the time, μ is the x-direction cosine of the photon direction of travel, and a, c, ρ, and c_v are the radiation constant, speed of light, material mass density, and material specific heat; σ_a, σ_s, and σ_t are the absorption, scattering, and total cross sections (cm^{-1}), respectively. The scalar radiation intensity $\phi(x,t) = \int_{-1}^{1} I(x,\mu,t)\mathrm{d}\mu$ is related to the radiation energy density E (with typical units Jks cm^{-3} sh^{-1}) by the relation $E = \phi/c$. The equations are strongly coupled through the gray Planckian emission source $\sigma_a ac T^4$, which is a nonlinear function of temperature, and the radiation absorption term $\sigma_a \phi$. In general, the material properties are a function of T. The temperature dependent material properties and absorption and reemission physics lead to systems that require accurate modeling of photon transport through a mix of streaming and optically-thick, diffusive regions. Although in most physical applications material motion is present, it is not the focus of this research and will not be considered. The purpose of the proposed research is to demonstrate the ability of a new algorithm to provide highly-accurate and efficient solutions to Eq. (5) and Eq. (6).

0.4.2 The implicit Monte Carlo method

The Monte Carlo (MC) method [?] is a standard computational method in the field of radiation transport. The implicit Monte Carlo (IMC) method [?] is the most common approach for applying the MC method to TRT problems. The IMC method partially linearizes Eq. (5) and Eq. (6) over a discrete time step and lags material properties to produce a linear transport equation, which can be solved with MC simulation. The linear transport equation contains an approximate emission source and effective scattering cross section that represent absorption and reemission of photons over a time step. The transport equation is solved with MC simulation to advance the distribution of radiation to the end of the time step and determine the energy absorbed by the material over the time step. The energy absorption by the material is

tallied over a discrete spatial mesh, computed with cell-averaged quantities. The energy absorption in each mesh cell is used to directly estimate a new end of time step material temperature based on the linearized material energy balance equation. Integration of the time-variable is treated continuously over the time step via MC sampling, but the linearized Planckian source in the transport equation is based on a time-discrete approximation.

The IMC method has some limitations. In optically thick regions, or for large time steps, the effective scattering dominates interactions. In these diffusive regions IMC becomes computationally expensive. Acceleration methods typically attempt to improve efficiency by allowing particles to take discrete steps through optically-thick regions based on a spatially-discretized diffusion approximation [?, ?]. Another issue occurs due to the approximate linearization of the system which can not be iteratively improved due to the high computational cost of the MC transport. For some problems, the linearization can yield non-physical results that violate the discrete maximum principle if the time step size is too large or the cell size is too small [?]. The violation of the maximum principle results in the material temperature being artificially higher than the boundary conditions and sources should physically allow. The violation is caused by the temperature in the emission source not being fully implicit in time due to the necessary linearization. The work in [?] uses less-expensive MC iterations to produce an implicit system which prevents this from happening, but has very slow iterative convergence in diffusive problems. In IMC, temperature-dependent material properties, in particular cross sections, are evaluated at the previous-time step temperature. These lagged cross sections can produce inaccurate solutions but do not cause stability issues.

For TRT simulations, inaccurate spatial representation of the emission source over a cell can result in energy propagating through the domain artificially fast, yielding non-physical results referred to as "teleportation error" [?]. The IMC method uses a fixup known as source tilting to mitigate this problem. Source tilting reconstructs a more accurate linear-discontinuous representation of the emission source within a cell based on the cell-averaged material temperatures in adjacent cells. This linear reconstruction is also necessary to preserve the asymptotic equilibrium diffusion limit (EDL), at least for a more general time step size and class of problems than for a piecewise constant representation [?]. Preserving the equilibrium diffusion limit is an important aspect of a numerical method for TRT problems. In this limit, cells are optically thick and diffusive, and the material and radiation energy

fields approach equilibrium. Spatial discretizations which do not preserve the EDL can produce inaccurate solutions, even though the mesh size should accurately capture the behavior of the solution [**?**].

0.4.3 Previous work on moment-based acceleration methods

An alternative application of MC to the TRT equations is moment-based hybrid MC methods. Recent work has focused on so-called high-order low-order (HOLO) methods [**?**, **?**, **?**, **?**]. These methods involve fixed-point iterations between high-order (HO) MC solution of a transport equation and a deterministic LO system. The low-order (LO) operator is based on angular moments of the transport equation, formulated over a fixed spatial mesh. Physics operators that are time consuming for MC to resolve, e.g., absorption-reemission physics, are moved to the LO system. The reduced angular dimensionality of the system and Newton methods allow for non-linearities in the LO equations to be fully resolved efficiently [**?**, **?**]. The high-order (HO) transport problem is defined by Eq. (5), with sources estimated from the previous LO solution. The high-order (HO) transport equation is solved via MC to produce a high-fidelity solution for the angular intensity. The MC estimate of the angular intensity is used to estimate consistency terms, present in the LO equations, that require the LO system to preserve the angular accuracy of the MC solution. These consistency terms are present in all spatial-regions of the problem, requiring statistical variance to be reduced sufficiently throughout the entire domain of the problem.

Another area of related research is the application of residual Monte Carlo. The goal of these methods is to solve an auxiliary transport equation for the error in some estimate of the intensity. The error is then added to the estimate of the solution, which can produce an overall solution for the intensity that has less statistical noise than solution of the original transport equation would produce. In [**?**], the MC simulation solves for the change in intensity from the previous time step. This has the potential to limit statistical noise significantly in regions where the solution is near equilibrium. The work in [**?**] used residual MC as a HO solver for 1D grey problems. The residual MC demonstrated impressive reduction in statistical variance. However, a piecewise constant representation was used for the space-angle representation of the intensity, which does not preserve the EDL and can be inaccurate

in angularly complex regions of the problem. Similar to RMC, a difference formulation has been applied to another algorithm known as the symbolic IMC method (SIMC), for the case of 1D frequency-dependent problems [**?**]. SIMC forms a standard FE solution to the material energy balance equation, and uses symbolic weights in the MC transport to solve for expansion coefficents. The difference formulation modifies the transport equation to solve for unknowns representing the deviation of the intensity from equilibrium with the material energy. The difference formulation was also applied to a linear-discontinuous FE spatial representation of the emission source, demonstrating accuracy in the EDL [**?**]. Both [**?**] and [**?**] produced minimal statistical noise in slowly varying problems where the behavior of the system is near equilibrium.

0.4.4 Proposed algorithm

The research proposed herein provides a new HOLO algorithm for radiative transfer. In this work, we propose an S_2-like LO operator [**?**] in conjunction with an exponentially-convergent MC (ECMC) method [**?**] for the HO solver. Our LO system and approach to enforcing consistency contrast greatly from the typical formulation in [**?, ?, ?**]. We have derived the LO operator directly from the transport equation, using a linear-discontinuous finite-element (LDFE) spatial discretization. Exponentially-convergent Monte Carlo (ECMC)[**?, ?**] provides an iterative algorithm that can efficiently reduce statistical noise to acceptable levels with significantly less particle histories than standard MC. In particular, ECMC is exceptionally efficient in time-dependent TRT problems because information about the intensity from the previous time step can be used as an accurate initial guess for the new end of time step intensity. However, implementation of ECMC is non-trivial, requiring a finite-element representation of the solution in all phase-space variables that are being sampled with MC. The method contains many of the desired qualities, such as preserving the equilibrium diffusion limit, preserving the maximum principle, and in particular, providing high-fidelity MC solution to the TRT equations in an efficient manner.

0.5 Performed Research

0.5.1 Overview of the HOLO Algorithm

For simplicity, our HOLO method uses a backwards Euler discretization in time, as well as constant specific heats and cell-wise constant cross sections. The time-discretized equations are

$$\mu\frac{\partial I^{n+1}}{\partial x} + \left(\sigma_t^{n+1} + \frac{1}{c\Delta t}\right) I^{n+1} = \frac{\sigma_s}{2}\phi^{n+1} + \frac{1}{2}\left(\sigma_a ac T^4\right)^{n+1} + \frac{I^n}{c\Delta t} \qquad (7)$$

$$\rho c_v \frac{T^{n+1} - T^n}{\Delta t} = \sigma_a^{n+1}\phi^{n+1} - \sigma_a ac(T^4)^{n+1}, \qquad (8)$$

where Δt is the uniform time step size, the superscript n is used to indicate the n-th time step. Cross sections are evaluated at the end of time step temperature, i.e., $\sigma_a^{n+1} \equiv \sigma_a(T^{n+1})$.

In the HOLO context, the LO solver models the physical scattering and resolves the material temperature spatial distribution $T^{n+1}(x)$, for each time step. The LO equations are formed via half-range angular and spatial moments of Eq. (7) and Eq. (8). The spatial moments are formed over a finite-element mesh and a linear-discontinuous spatial closure with upwinding is used to close the system. The angular treatment in the LO equations has the same form as those used in the hybrid-S_2 method in [?], with consistency parameters that represent angularly-weighted averages of the intensity. If the angular consistency parameters were estimated exactly, then the LO equations preserve the exact angular-averaged solution, neglecting spatial discretization errors. These consistency parameters are lagged in each LO solve, estimated from the previous HO solution for the intensity, or from a previous time step. The discrete LO equations always conserve total energy, independent of the accuracy of the consistency terms. It is noted that our LO operator is different from the nonlinear diffusion acceleration (NDA) methods used by other HOLO methods [?, ?, ?]. In NDA methods, an artificial term is added to the LO equations to enforce consistency and estimated using a previous HO solution. In our method we have simply algebraically manipulated space-angle moment equations to produce our consistency terms, which will hopefully produce more stability in optically-thick regions where NDA methods demonstrate stability issues.

The solution to the LO system is used to construct a LDFE spatial representation of the scattering and emission sources on the right hand side of

11

Eq. (7). This HO transport problem represents a characteristic method that uses MC to invert the continuous streaming plus removal operator with an LDFE representation of sources. We will solve this transport problem using ECMC [**?**]. The output from ECMC is $\tilde{I}^{n+1}(x, \mu)$, a space-angle LDFE projection of the exact solution for $I^{n+1}(x, \mu)$. Once computed, $\tilde{I}^{n+1}(x, \mu)$ is used to directly evaluate the necessary consistency parameters for the next LO solve. The HO solution is not used to directly estimate a new material temperature, which eliminates typical operator splitting stability issues that require linearization of the emission source in Eq. (5).

The process of performing subsequential HO and LO solves, within a single time step, can be repeated to obtain an increasingly accurate solution for $\phi^{n+1}(x)$ and $T^{n+1}(x)$. Thus, the HOLO algorithm, for the n-th time step, is

1. Perform a LO solve to produce an initial guess for $T^{n+1}(x)$ and $\phi^{n+1}(x)$, based on consistency terms estimated with $\tilde{I}^n$.

2. Solve the HO system with ECMC for $\tilde{I}^{n+1}(x, \mu)$, based on the current LO estimate of emission and scattering sources.

3. Compute new LO consistency parameters with $\tilde{I}^{n+1}$.

4. Solve the LO system with HO consistency parameters to produce a new estimate of ϕ^{n+1} and T^{n+1}.

5. Optionally repeat $2 - 4$ until desired convergence is achieved.

6. Store $\tilde{I}^n \leftarrow \tilde{I}^{n+1}$, and move to the next time step.

The consistency terms force the HO and LO solutions for $\phi^{n+1}(x)$ to be consistent to the order of the current HOLO iteration error, as long as the LDFE spatial representation can accurately represent $\phi(x)$ and $T(x)$.

0.5.2   The Low-Order Equations

This section contain explicit details of the LO operator. To form the LO system of equations, spatial moments are taken over each spatial cell i: $x \in [x_{i-1/2}, x_{i+1/2}]$, weighted with the standard linear finite element (FE)

interpolatory basis functions. For example, the L moment operator is defined by

$$\langle \cdot \rangle_{L,i} = \frac{2}{h_i} \int_{x_{i-1/2}}^{x_{i+1/2}} b_{L,i}(x)(\cdot)\mathrm{d}x, \tag{9}$$

where $h_i = x_{i+1/2} - x_{i-1/2}$ is the width of the spatial element and $b_{L,i}(x) = (x_{i+1/2} - x)/h_i$ is the FE basis function, for cell i, corresponding to position $x_{i-1/2}$. The right moment $\langle \cdot \rangle_{R,i}$ is defined with weight function $b_{R,i}(x) = (x - x_{i-1/2})/h_i$. To reduce the angular dimensionality, positive and negative half-range integrals of the angular intensity are taken. The half-range averages of I are defined as $\phi^+(x) = \int_0^1 I(x,\mu)\mathrm{d}\mu$ and $\phi^-(x) = \int_{-1}^0 I(x,\mu)\mathrm{d}\mu$, respectively. Thus, in terms of half-range quantities, $\phi(x) = \phi^-(x) + \phi^+(x)$.

Pairwise application of the L and R basis moments with the $+$ and $-$ half-range integrals to Eq. (7) ultimately yields four moment equations per cell. As in [?], algebraic manipulation is performed to form intensity-weighted averages of μ, which we denote consistency terms. As an example, the equation resulting from application of the L moment and positive half-range integral is

$$-2\mu_{i-1/2}^{n+1,+}\phi_{i-1/2}^{n+1,+} + \{\mu\}_{L,i}^{n+1,+}\langle\phi\rangle_{L,i}^{n+1,+} + \{\mu\}_{R,i}^{n+1,+}\langle\phi\rangle_{R,i}^{n+1,+} + \left(\sigma_{t,i}^{n+1} + \frac{1}{c\Delta t}\right)h_i\langle\phi\rangle_{L,i}^{n+1,+}$$

$$-\frac{\sigma_{s,i}h_i}{2}\left(\langle\phi\rangle_{L,i}^{n+1,+} + \langle\phi\rangle_{L,i}^{n+1,-}\right) = \frac{h_i}{2}\langle\sigma_a^{n+1}acT^{n+1,4}\rangle_{L,i} + \frac{h_i}{c\Delta t}\langle\phi\rangle_{L,i}^{n,+}, \tag{10}$$

where the $\phi_{i-1/2}^+$ and $\mu_{i-1/2}^+$ terms represent face-averaged quantities at $x_{i-1/2}$. The negative direction and R moment equations are derived analogously. The element-averaged angular consistency terms are defined in terms of half-range integrals, e.g.,

$$\{\mu\}_{L,i}^{n+1,+} \equiv \frac{\langle\mu I^{n+1}\rangle_{L,i}^+}{\langle I^{n+1}\rangle_{L,i}^+} = \frac{\frac{2}{h_i}\int\limits_0^1\int\limits_{x_{i-1/2}}^{x_{i+1/2}}\mu\, b_{L,i}(x)I^{n+1}(x,\mu)\mathrm{d}x\mathrm{d}\mu}{\frac{2}{h_i}\int\limits_0^1\int\limits_{x_{i-1/2}}^{x_{i+1/2}}b_{L,i}(x)I^{n+1}(x,\mu)\mathrm{d}x\mathrm{d}\mu}. \tag{11}$$

The $\mu_{i-1/2}^{n+1,+}$ term is defined analogously and represents an angular average on the face at $x_{i-1/2}$.

To derive the LO material energy equations, $T(x)$ is represented spatially in the LDFE trial space, i.e., $T(x) \simeq T_{L,i}b_{L,i}(x) + T_{R,i}b_{R,i}(x), \quad x \in$

13

$(x_{i-1/2}, x_{i+1/2})$. Similarly, the emission term is represented in the material and radiation equations with the LDFE interpolant $T^4(x) \simeq T_{L,i}^4 b_{L,i}(x) + T_{R,i}^4 b_{R,i}(x)$. The L and R spatial moments are taken of the material energy equation, using these definitions for $T(x)$ and $\sigma_a ac T^4(x)$ to simplify moments. For example, the final LO material energy equation resulting from application of the L moment is

$$\frac{\rho_i c_{v,i}}{\Delta t} \left[\left(\frac{2}{3}T_{L,i} + \frac{1}{3}T_{R,i}\right)^{n+1} - \left(\frac{2}{3}T_{L,i} + \frac{1}{3}T_{R,i}\right)^n \right] + \sigma_{a,i}^{n+1} \left(\langle\phi\rangle_{L,i}^+ + \langle\phi\rangle_{L,i}^-\right)^{n+1}$$
$$= \sigma_{a,i}^{n+1} ac \left(\frac{2}{3}T_{L,i}^4 + \frac{1}{3}T_{R,i}^4\right)^{n+1}. \quad (12)$$

Cross sections have been assumed constant over each element, evaluated at the average temperature within the element, i.e., $\sigma_{a,i}^{n+1} = \sigma_{a,i}([T_{L,i}^{n+1} + T_{R,i}^{n+1}]/2)$.

0.5.3 Closing the LO equations

The six degrees of freedom (DOF) over each cell i are the four moments $\langle\phi\rangle_{L,i}^+$, $\langle\phi\rangle_{R,i}^+$, $\langle\phi\rangle_{L,i}^-$, and $\langle\phi\rangle_{R,i}^-$ and the two spatial edge values $T_{L,i}$ and $T_{R,i}$. The relation between the volume and face averaged quantities and the angular consistency parameters (e.g., Eq. (19)) are not known a priori. Currently, to close the LO system spatially, the standard LDFE approximation with upwinding is used. For example, for positive flow (e.g., Eq. (18)) the face terms $\mu_{i-1/2}$ and $\phi_{i-1/2}$ are upwinded from the previous cell $i-1$ or from a boundary condition; the terms at $x_{i+1/2}$ are linearly extrapolated, computed using the L and R basis moments, e.g., $\phi_{i+1/2}^+ = 2\langle\phi\rangle_R^+ - \langle\phi\rangle_L^+$. We will investigate using the HO solution to estimate the spatial closure, as discussed in Sec. 0.6 A lagged estimate of I^{n+1} from the latest HO solve is used to estimate the angular consistency parameters.

0.5.4 Solution of the LO equations

Newton's method is used to solve the global system of coupled LO equations, based on a typical linearization of the Planckian source with cross sections evaluated at lagged temperatures. This procedure is described in [?]. Once the system is linearized, a discrete matrix equation is formed. Scattering (including the effective scattering resulting from the linearization of

14

the Planckian source) can be included in the system matrix, producing an asymmetric, banded-matrix. The matrix has a band width of seven and is inverted directly. Newton iterations are repeated until $\phi^{n+1}(x)$ and $T^{n+1}(x)$ are converged to a desired relative tolerance.

0.5.5 The ECMC High Order Solver

The transport equation to be solved by the HO solver is

$$\mu\frac{\partial I^{n+1}}{\partial x} + \left(\sigma_t + \frac{1}{c\Delta t}\right)I^{n+1} = \frac{\sigma_s}{2}\phi_{LO}^{n+1} + \frac{1}{2}\left(\sigma_a acT_{LO}^4\right)^{n+1} + \frac{\tilde{I}^n}{c\Delta t}, \quad (13)$$

where the emission and scattering sources are known from the previous LO solution and $\tilde{I}^n$ is the LDFE projection of $I(x,\mu)$ from the previous time step. This defines a fixed-source, pure absorber transport problem that must be solved for each HO solve. In operator notation, Eq. (21) can be written as

$$\mathbf{L}I^{n+1} = q \quad (14)$$

where I^{n+1} is the exact transport solution for the end-of-time-step intensity. The linear operator $\mathbf{L}$ is the streaming plus removal operator defined by the left hand side of Eq. (7). The m-th approximate LDFE solution to Eq. (22) (m is the index of inner HO batches) is represented as $\tilde{I}^{n+1,(m)}$. The m-th residual is defined as $r^{(m)} = q - \mathbf{L}\tilde{I}^{n+1,(m)}$. Addition of $\mathbf{L}I^{n+1} - q = 0$ to the residual equation and manipulation of the result yields the error equation

$$\mathbf{L}(I^{n+1} - \tilde{I}^{n+1,(m)}) = \mathbf{L}\epsilon^{(m)} = r^{(m)} \quad (15)$$

where I^{n+1} is the exact solution and $\epsilon^{(m)}$ is the error in $\tilde{I}^{n+1,(m)}$. We have suppressed the HOLO iteration indices because the LO estimated q^k and $\mathbf{L}^k$ remain constant over the entire HO solve. The $\mathbf{L}$ operator in the above equation is inverted yielding the Monte Carlo LDFE projection of the error in $\tilde{I}^{n+1,(m)}$, i.e.,

$$\tilde{\epsilon}^{(m)} = \mathbf{L}^{-1}r^{(m)} \quad (16)$$

where $\mathbf{L}^{-1}$ is the inversion of the streaming and removal operator via MC simulation. The fundamental transport of particles is the same as standard MC particle transport codes, but the LDFE source will now contain positive and negative weight particles. The space-angle moments of the computed

15

error $\tilde{\epsilon}^{(m)}$ can be added to the moments of $\tilde{I}^{n+1,(m)}$ to produce a more accurate solution.

Here, we emphasize the solution $\tilde{I}^{n+1,(m)}$ represents the projection of the exact Monte Carlo solution onto the LDFE trial space. This is in general far more accurate than a standard finite element solution, particularly in the angular variable. For example, in typical IMC calculations the average energy deposition within a cell is computed using a standard path-length volumetric flux tally; the zeroth moment of the LDFE projection of $\tilde{\epsilon}$ is computed using an equivalent tally. The primary truncation error is in the LD spatial representation of the source term q. Volumetric flux tallies over each space-angle element are required to represent $\tilde{\epsilon}^{(m)}$.

The ECMC algorithm is

1. Initialize guess for $\tilde{I}^{n+1,(0)}$ to $\tilde{I}^n$ or the projection of $\tilde{I}^{n+1}$ from the latest HO solve

2. Compute $r^{(m)}$.

3. Perform a MC simulation to obtain $\tilde{\epsilon}^{(m)} = \mathbf{L}^{-1} r^{(m)}$

4. Compute a new estimate of the intensity $\tilde{I}^{n+1,(m+1)} = \tilde{I}^{n+1,(m)} + \tilde{\epsilon}^{(m)}$

5. Repeat steps 2 – 4 until desired convergence criteria is achieved.

The initial guess for the angular intensity $I^{n+1,(0)}$ is computed based on the previous solution for $\tilde{I}^n$. This is a critical step in the algorithm; it significantly reduces the required number of particles per time step because the intensity does not change drastically between time steps in optically thick regions. Exponential convergence is obtained because with each batch a better estimate of the solution is being used to compute the new residual, decreasing the magnitude of the MC residual source each iteration m, relative to the solution I^{n+1}. Each MC estimate of the moments of ϵ still has a statistical uncertainty that is governed by the standard $1/\sqrt{N}$ convergence rate [?], for a particular source $r^{(m)}$, where N is the number of histories performed. If the statistical estimate of the projection $\tilde{\epsilon}$ is not sufficiently accurate, then the iterations would diverge.

Because the exact angular intensity does not in general lie within the LDFE trial space, the iterative estimate of the error will eventually stagnate once the error cannot be sufficiently represented by a given FE mesh. An adaptive $h-$refinement algorithm has been implemented that can be used to

allow the system to continue converging towards the exact solution [**?**, **?**]. In general, for TRT problems, optically thick and slowly varying regions of the problem do not require as refined of a mesh as neutronics calculation to accurately capture the solution because there is less variation in the angular dependence of the solution. It is noted the adaptive refinement is only applied to the HO mesh; the LO spatial mesh is fixed.

We have applied some basic variance reduction techniques. Because we are solving a pure absorber problem with Monte Carlo, we will allow particles to stream without absorption to reduce statistical variance in the tallies. The weight of particles is reduced deterministically along the path as they stream, with no need to sample a path length. Another implemented variance reduction is biased source sampling locations. The goal is to effectively distribute particle histories to regions of importance, but to sample a minimum number of histories in less probable regions to prevent large statistical noise. However, there is no need to sample histories where the solution is in equilibrium. The importance sampling is performed using a modified systematic sampling method [**?**].

0.5.6 Computational Results

The research described thus far has been implemented in a stand alone research code. To demonstrate the efficacy of our algorithm, we provide results of our HOLO algorithm for two Marshak wave test problems. Marshak wave problems provide a standard test for computational methods in radiative transfer. For the first problem, the radiation and material energies are initially in equilibrium at a cold temperature. A large, isotropic incident intensity is applied at $x = 0$. The absorption cross section varies as $\sigma(T) = 0.001 \ \rho \ T^{-3} \ (\text{cm}^{-1})$. The simulation is advanced until $t = 5$ sh $(1 \text{ sh} \equiv 10^{-8} \text{ s})$ with a fixed time step size of 0.001 sh. We have performed no mesh refinement, only performed one HOLO iteration per time step, and used a fixed 3 HO batches with equal number of histories per batch. Radiation energy distributions are plotted as an equivalent temperature given by $T_r = (\phi/(ac))^{0.25}$. Cell-averaged quantities are plotted.

Fig. 3a compares the cell-averaged radiation temperatures for IMC with source tilting and the HOLO method with ECMC, for various number of spatial mesh cells N_c; we have used HOLO-ECMC to denote our algorithm because later results will use different HO solvers. The IMC and HOLO solutions agree as the mesh is converged. Fig. 3b compares solutions for the

17

case of 200 cells. The HOLO method demonstrates significantly less statistical noise, even though it used fewer histories per time step. To prevent negativities in the LO equations, a modified spatial closure was used that is equivalent to the standard FE lumping procedure. This lumping-equivalent closure and S_2 equivalent consistency terms are applied in cells where negative values occur to ensure positivity. An alternative approach to resolving negativities is proposed in Sec. 0.6.1.
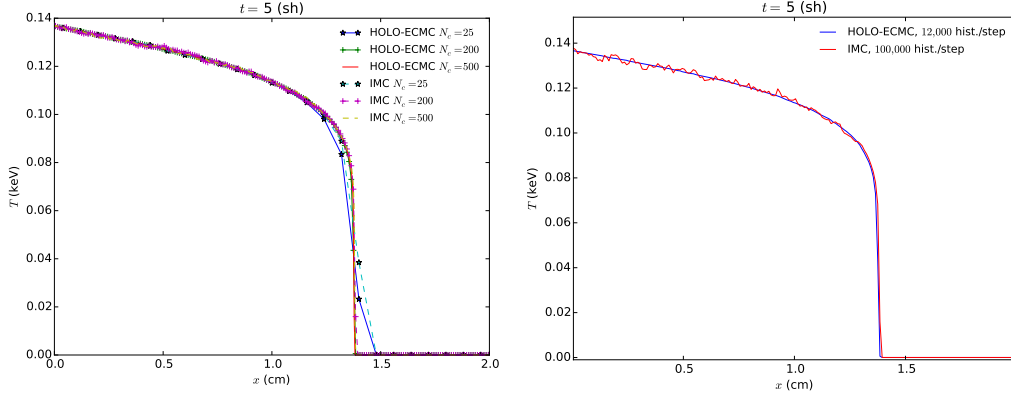
(a) Spatial convergence of IMC and HOLO.

(b) Comparison of solutions for 200 spatial cells.

Figure 1: **Comparison of radiation temperatures for Marshak wave problem at t = 5 sh.**

The second problem has similar behavior to the first problem, however the geometry consists of an optically thin (left) and an optically thick (right) material region, with temperature-independent cross sections. Fig. 4a compares the HOLO and IMC radiation temperatures at the end of the simulation. The IMC and HOLO results show good agreement over the finer mesh. On the coarse mesh ($N_c = 20$), the LDFE representation of T^4 in the HOLO method predicts the location of the wave front more accurately than the source tilting of the IMC method. Fig. 4b demonstrates the benefit of ECMC as a HO solver compared to standard MC. The HOLO algorithm with the ECMC HO solver (HOLO-ECMC) results are for running 3 batches of 10,000 histories, per time step. The solution for the HOLO method with a standard MC solver as the HO solver (HOLO-SMC) with standard source sampling uses 10^5 histories per time step. The HOLO-SMC solution demonstrates

18

significant statistical noise. This noise is introduced into the LO solver by poor statistics in the MC computed consistency terms. Also plotted is an S_2 solution obtained with consistency terms that are equivalent to S_2 and no HO correction. The S_2 solution results in an artificially fast wave front, as expected, demonstrating the necessity of HO correction in this problem.
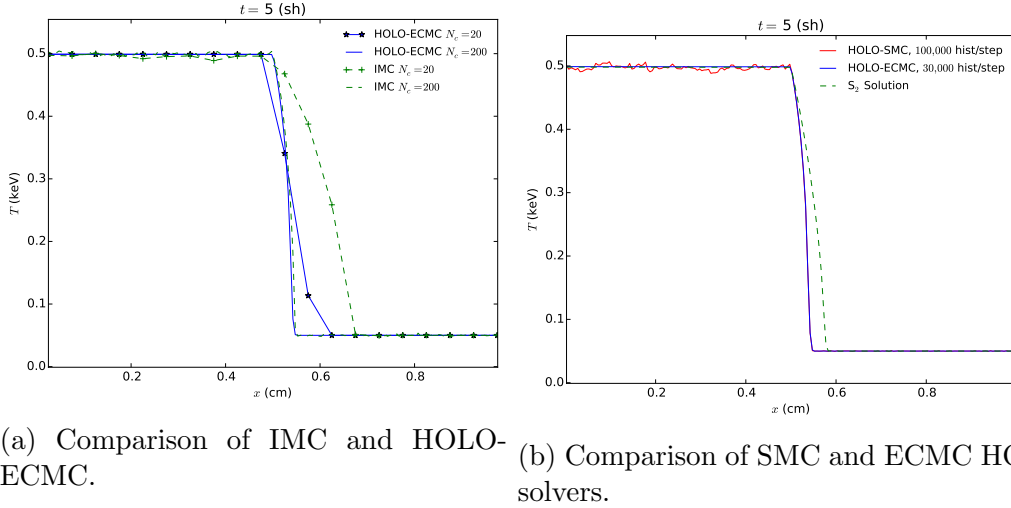

(a) Comparison of IMC and HOLO-ECMC.

(b) Comparison of SMC and ECMC HO solvers.

Figure 2: **Comparison of radiation temperatures for two material problem.**

0.6 Discussion of Remaining Research

0.6.1 Resolving Issues in Optically Thick Cells

The linear-discontinuous (LD) closure with upwinding is not strictly positive. In particular, for optically thick cells with a steep intensity gradient, the intensity becomes negative. In typical TRT problems (e.g., the Marshak wave problems above), this negativity occurs at the wave-front of the radiation intensity in optically thick materials. These negativities are not physical and can propagate to adjacent cells. In thick regions of TRT problems, reasonably fine spatial cells can still be on the order of millions of mean free paths; negativities with an LD representation are unavoidable in practice for such cells, and mesh refinement is of minimal use. We will explore several methods for resolving negativities. Ideally the solutions in such cells should

19

be as consistent as possible for the HO and LO equations. However, the differences between the solution methods of the two equations, as well as the fact that some terms are lagged, have lead to the development of independent approaches for the LO and HO systems thus far.

Typically, for a standard LDFE method, the equations are lumped to produce a strictly positive solution (for 1D) [**?**]. However, standard FE lumping procedures would introduce difficulties in computing the consistency terms from the HO solution. The results in Sec. 0.5.6 used a lumping-equivalent closure for the LO equations and S_2 equivalent angular terms.. This approach will not produce accurate results for general problems in higher spatial dimensions. Also, a lumping equivalent closure in x does not guarantee positivity for the space-angle LDFE representation of the HO intensity. Alternatively, the equations within a cell can be modified to ensure the outflow is not below the floor value (the initial temperature of the problem), and energy balance is conserved. The LD shape is reconstructed by extrapolating from the outflow back through the average. This closure has been implemented and is more promising for extendability into higher dimensions.

For the HO solver, after an ECMC batch, we detect cells that produced a negative intensity. In these cells, we scale the linear representation of the intensity (in x and μ) to be greater than the floor value. This scaling process of the two moments is underdefined, so there is not a unique way to enforce positivity. The scaling procedure is not an emphasis of the research, so we apply the simple approach of scaling the slopes such that the ratio of the slope in x and μ is unchanged. The scaled intensity will not satisfy the original residual equation accurately because we have modified the first moments. Thus, the ECMC error estimates will rapidly stagnate, and produce relatively inaccurate solutions. This scaling can also lead to negativities in down-stream cells that is unphysical in later batches. To mitigate stagnation and improve accuracy, we will add an artifical source $\tilde{\delta}^{m+1}(x, \mu)$ to the HO equation. This source is estimated iteratively as

$$\tilde{\delta}(x, \mu)^{(m+1)} = \mathbf{L}(\tilde{I}^{n+1,(m)} - \tilde{I}_{\text{pos}}^{n+1,(m)}),$$

where $\tilde{I}_{pos}^{n+1}$ is the modified positive solution. Essentially, this source is modifying the first moments of the transport equation to ensure a positive solution within the negative cells. If necessary, we can estimate a new source again in the next batch. The source $\tilde{\delta}$ lies in the same functional space as the residual, and thus can use the existing code for computing the residual and will be straight forward to extend to higher dimensions.

We have implemented this artificial source and found it to reduce the magnitude of the MC estimated error, producing a positive solution. We still need to investigate the accuracy and robustness of the added source method, and whether it should be recomputed every batch, once it has been triggered, or only when the solution becomes negative again. We will also investigate adding the source to the LO equations for greater consistency and accuracy in the LO equations. This will not necessarily guarantee positivity in the LO equations due to the lagged estimate of the emission source in used in the previous HO solution. We will investigate altering the method for computing the added source computation to ensure the zeroth moment of the equations is not changed, ensuring energy conservation.

0.6.2 Estimating the Spatial Closure from the HO Solution

We will explore the possibility of a linear, doubly-discontinuous trial space in in the HO and LO equations. This trial space allows the outflow from a cell to be discontinuous in space, introducing extra unknowns. The linear shape on the interior of the cell is still used to represent the temperature unknowns, scattering source, and emission source. The choice of this trial space should allow for higher consistency between the HO and LO equations by using MC to compute outflows from space-angle cells, rather than an LD extrapolation of the solution. For the HO solution, a discontinuous outflow for a space-angle cell should produce greater angular accuracy on faces. In optically thick cells, this will mitigate observed issues with the spatial slope being artificially high to account for the discrepancy in angular shape between the internal and face solutions. The outflow will be estimated using a face-based tally of the MC solution. The error equation can be modified to estimate the outflow for a given batch. For the LO equations, a parametric relation between the outflow and internal moments, as estimated by the latest HO solution, will be used to eliminate the extra unknowns. This will produce a consistent spatial closure between the HO and LO solutions upon convergence. The closure relation will be averaged over each half-range, similar to the angular consistency parameters. Poor statistics for the face tallies may result in this trial space producing less accurate results compared to the standard LDFE solution, at least for sufficiently fine meshes where LD can accurately represent the solution. Although the closure will be applied everywhere, we

expect the greatest improvement in accuracy for cells where the LDFE trial space produces a negative solution.

0.6.3   Diffusion Synthetic Acceleration of the LO Equations

As described in Sec. 0.5.4, the fully-discretized LO equations can include the scattering term in the system matrix. This allows for the system to be directly inverted. However, the S_2 like system cannot be efficiently inverted directly in higher spatial dimensions. To demonstrate a possible path forward in higher dimensions, we will investigate the use of a standard source iteration scheme to solve the LO equations. As material properties become more diffusive (e.g., c_v is small and σ_a is large), the effective scattering source becomes large. This results in a spectral radius of the source iterations that approaches unity [?]. These regimes are typical in TRT simulations, so an acceleration method is critical. We will accelerate the source iterations with a nearly-consistent diffusion synthetic acceleration (DSA) method [?, ?].

We can perform standard source iterations by lagging the scattering source in the LO equations, which uncouples unknowns between the two half-ranges. This produces a lower-triangular system where the spatial unknowns can be determined sequentially along the two directions of flow via a standard sweeping procedure [?, ?]. The newly computed half-range intensities can be used to compute the scattering source for the next iteration. This process is repeated until convergence. A form of DSA referred to as the WLA method is used to accelerate the source iterations [?]. Between each source iteration, a residual equation is formed that provides the error in the current scattering iteration. The DSA method uses an approximate, lower-order operator to estimate the error in the zeroth angular moment of the intensity. The DSA equations can be more efficiently solved than the S_2-like sweeps that are being accelerated, but will accurately resolve the slowly converging diffusive error modes. It is important for the spatial discretization of the DSA equations to be closely related to the discretization of the LO equations for the acceleration to be effective. The WLA method first solves a spatially-continuous discretization of the diffusion equation for the iterative error on faces. The error on the faces is then mapped onto the volumetric moment unknowns via a LD discretization of diffusion equation [?]. The LD mapping resolves issues that would occur in optically-thick cells, while the

continuous diffusion equation is accurate in the EDL where acceleration is important.

We have implemented the DSA algorithm and initial results indicate that the acceleration is effective. However, we have only considered the case when the LO equations and DSA equations are lumped. We will investigate the effect of acceleration when alternative negativity fix-ups are implemented that result in DSA and LO equations that are not spatially consistent. We will recast the DSA method as a preconditioner to an iterative Krylov solution [**?**] of the LO equations if acceleration degrades. Generally, Krylov methods mitigate acceleration losses due to inconsistencies in the acceleration method. In higher dimensions, the use of a Krylov method is necessary for effective acceleration for nearly-consistent acceleration methods such as WLA in problems with mixed optical thicknesses [**?**], e.g., typical radiative transfer problems. We would apply the preconditioned-Krylov approach to allow for the use of lumped DSA equations as a preconditioner, with the LO equations using one of the other fixup approaches detailed in the previous section. It is noted we are not interested in measuring the reduction of computational time because in 1D the LO equations can be directly solved efficiently. We are just interested in ensuring that DSA or a preconditioned-Krylov methods can reduce the number of scattering iterations sufficiently, including cases where inconsistencies in the LO equations are present.

0.7 Summary and Outline of Remaining Research

A new HOLO algorithm has been implemented, and results have demonstrated the ability to reproduce IMC solutions accurately for two difficult Marshak wave test problems. The ECMC approach, with initial guesses based on the previous radiation intensity, results in efficient reduction of statistical error and allows for particles to be distributed to largely varying regions of the problem. The LO solver resolves the non-linearities in the equations resulting in a fully implicit time discretization. Overall, the LO solver can accurately and efficiently resolve the solution in diffusive regions, while the HO transport solver provides the accuracy of a full transport treatment where necessary.

We have proposed solutions to resolve issues in optically-thick cells and a

source iteration method for demonstrating the efficacy of our method. The ability to overcome rapid stagnation in the ECMC algorithm when the solution cannot be accurately represented by the trial space, e.g., negativities in optically thick cells, will be key for generalization of this method to higher dimensions. The goal of our proposed fixup is to mitigate the rapid stagnation of ECMC iterations that would occur by forcing a positive solution each batch. Ideally, the added source will reduce the stagnation to order of the global stagnation that occurs in other regions of the problem due to mesh resolution and a finite number of histories per batch. The LO and HO solutions will independently resolve issues with negativities, with the goal of producing as consistent and accurate of solutions as possible. We also need to numerically demonstrate the ability of DSA to accelerate our LO equations, in conjunction with a iterative Krylov solution method. There are other desirable properties of our algorithm that remain to be tested, e.g., preservation of the maximum principle. In summary, we propose performing the following work to complete this dissertation research:

1. The source iteration method with DSA for the LO solver will be applied to various test problems to ensure a significant reduction in total scattering iterations and the numerically estimated spectral radius in diffusive problems. Problems that provide a mix of optically thick and thin regions, particularly those that require the fix-ups defined in Sec. 0.6.1 where acceleration may degrade, will be investigated. The acceleration method will be recast as a DSA-preconditioned Krylov method if required for robustness and effectivness.

2. Problems where IMC violates the maximum principle will be simulated with our method. We will demonstrate that our implicit equations preserve the maximum principle, and that our method can produce higher accuracy due to implicit cross section treatment. Such problems will likely require implementation of damping in the Newton iterations.

3. We will numerically demonstrate the ability of our method to preserve the equilibrium diffusion limit. The HOLO method will also be tested with a step discretization in the LO equations to demonstrate inaccuracy in the EDL.

4. The negativity fix-ups discussed in Sec. 0.6.1 will be investigated for robustness and accuracy. An analytic neutronics problem or a refined

24

deterministic TRT solution will be used to test for accuracy. The ability of the modified ECMC algorithm to reduce noise in the fixup regions will be investigated by measuring sample statistics.

5. The doubly-discontinuous trial space with a consistent spatial closure in the LO equations remains to be implemented. This approach will be compared to the standard LD closure for accuracy, particularly in the case of negative cells.

6. We will investigate the sensitivity of ECMC and the LO equations to parameters, e.g., initial mesh-sizes, adaptive refinement, time step size, history counts, and batch sizes. Additional test problems will be simulated as necessary.

0.8 Forming the Low-Order System

To form the LO system of equations, spatial moments are taken over each spatial cell i: $x \in [x_{i-1/2}, x_{i+1/2}]$, weighted with the standard linear finite element (FE) interpolatory basis functions. For example, the L moment operator is defined by

$$\langle \cdot \rangle_{L,i} = \frac{2}{h_i} \int_{x_{i-1/2}}^{x_{i+1/2}} b_{L,i}(x)(\cdot)\mathrm{d}x, \tag{17}$$

where $h_i = x_{i+1/2} - x_{i-1/2}$ is the width of the spatial element and $b_{L,i}(x) = (x_{i+1/2} - x)/h_i$ is the FE basis function, for cell i, corresponding to position $x_{i-1/2}$. The right moment $\langle \cdot \rangle_{R,i}$ is defined with weight function $b_{R,i}(x) = (x - x_{i-1/2})/h_i$. It is noted in this notation $\langle \phi \rangle_{L,i}$ and $\langle \phi \rangle_{R,i}$ represent spatial moments of the intensity over cell i, opposed to $\phi_{L,i}$ and $\phi_{R,i}$, which represent the interior value of the linear representation of $\phi(x)$ at $x_{i-1/2}$ and $x_{i+1/2}$ within the cell. To reduce the angular dimensionality, positive and negative half-range integrals of the angular intensity are taken. The half-range averages of I are defined as $\phi^+(x) = \int_0^1 I(x, \mu)\mathrm{d}\mu$ and $\phi^-(x) = \int_{-1}^0 I(x, \mu)\mathrm{d}\mu$, respectively. Thus, in terms of half-range quantities, $\phi(x) = \phi^-(x) + \phi^+(x)$.

0.8.1 Radiation Energy Equations

Pairwise application of the L and R basis moments with the $+$ and $-$ half-range integrals to Eq. (7) ultimately yields four moment equations per cell. As in [?], algebraic manipulation is performed to form intensity-weighted averages of μ, which we denote as consistency terms. As an example, the equation resulting from application of the L moment and positive half-range integral is

$$-2\mu_{i-1/2}^{n+1,+} \phi_{i-1/2}^{n+1,+} + \{\mu\}_{L,i}^{n+1,+} \langle \phi \rangle_{L,i}^{n+1,+} + \{\mu\}_{R,i}^{n+1,+} \langle \phi \rangle_{R,i}^{n+1,+} + \left(\sigma_{t,i}^{n+1} + \frac{1}{c\Delta t}\right) h_i \langle \phi \rangle_{L,i}^{n+1,+}$$

$$- \frac{\sigma_{s,i} h_i}{2} \left(\langle \phi \rangle_{L,i}^{n+1,+} + \langle \phi \rangle_{L,i}^{n+1,-}\right) = \frac{h_i}{2} \langle \sigma_a^{n+1} ac T^{n+1,4} \rangle_{L,i} + \frac{h_i}{c\Delta t} \langle \phi \rangle_{L,i}^{n,+}, \tag{18}$$

where the $\phi_{i-1/2}^+$ and $\mu_{i-1/2}^+$ terms represent face-averaged quantities at $x_{i-1/2}$. The negative direction and R moment equations are derived analogously. The element-averaged angular consistency terms are defined in terms of half-range

integrals, e.g.,

$$\{\mu\}_{L,i}^{n+1,+} \equiv \frac{\langle \mu I^{n+1}\rangle_{L,i}^+}{\langle I^{n+1}\rangle_{L,i}^+} = \frac{\frac{2}{h_i}\int\limits_0^1 \int\limits_{x_{i-1/2}}^{x_{i+1/2}} \mu\, b_{L,i}(x) I^{n+1}(x,\mu)\mathrm{d}x\mathrm{d}\mu}{\frac{2}{h_i}\int\limits_0^1 \int\limits_{x_{i-1/2}}^{x_{i+1/2}} b_{L,i}(x) I^{n+1}(x,\mu)\mathrm{d}x\mathrm{d}\mu}. \tag{19}$$

The $\mu_{i-1/2}^{n+1,+}$ term is defined analogously and represents an angular average on the face at $x_{i-1/2}$.

0.8.2 Material Energy Equations

To derive the LO material energy equations, $T(x)$ is represented spatially in the LDFE trial space, i.e., $T(x) \simeq T_{L,i}b_{L,i}(x) + T_{R,i}b_{R,i}(x)$, $x \in (x_{i-1/2}, x_{i+1/2})$. Similarly, the emission term is represented in the material and radiation equations with the LDFE interpolant $T^4(x) \simeq T_{L,i}^4 b_{L,i}(x) + T_{R,i}^4 b_{R,i}(x)$. The L and R spatial moments are taken of the material energy equations; the LDFE representations for $T(x)$ and $\sigma_a ac T^4(x)$ are used to simplify the spatial integrals. For example, the final LO material energy equation resulting from application of the L moment is

$$\frac{\rho_i c_{v,i}}{\Delta t}\left[\left(\frac{2}{3}T_{L,i} + \frac{1}{3}T_{R,i}\right)^{n+1} - \left(\frac{2}{3}T_{L,i} + \frac{1}{3}T_{R,i}\right)^n\right] + \sigma_{a,i}^{n+1}\left(\langle\phi\rangle_{L,i}^+ + \langle\phi\rangle_{L,i}^-\right)^{n+1}$$
$$= \sigma_{a,i}^{n+1} ac\left(\frac{2}{3}T_{L,i}^4 + \frac{1}{3}T_{R,i}^4\right)^{n+1}. \tag{20}$$

Cross sections have been assumed constant over each element, evaluated at the average temperature within the element, i.e., $\sigma_{a,i}^{n+1} = \sigma_{a,i}([T_{L,i}^{n+1} + T_{R,i}^{n+1}]/2)$. Because the material energy balance only contains angularly integrated quantities, there is no need to take angular moments of the above equation.

0.8.3 Closing the System with Information from the HO solution

The six degrees of freedom (DOF) over each cell i are the four moments $\langle\phi\rangle_{L,i}^+$, $\langle\phi\rangle_{R,i}^+$, $\langle\phi\rangle_{L,i}^-$, and $\langle\phi\rangle_{R,i}^-$ and the two spatial edge values $T_{L,i}$ and $T_{R,i}$. The

four radiation and two material energy equations define a system of equations for the six DOF, coupled to other cells via upwinding in the streaming term. The relation between the volume and face averaged quantities and the angular consistency parameters (e.g., Eq. (19)) are not known a priori. A lagged estimate of I^{n+1} from the previous HO solve is used to estimate the angular consistency parameters. In the HOLO algorithm, the equations for LO unknowns at iteration $k+1$ use consistency parameters computed (via relations, e.g., Eq. (19)) using the latest HO solution $\tilde{I}^{n+1,k+1/2}$ as an approximation for $I^{n+1}(x,\mu)$. To close the LO system spatially, a linear-discontinuous (LD) spatial closure with the usual upwinding approximation is used. For example, for positive flow (e.g., Eq. (18)) the face terms $\mu_{i-1/2}$ and $\phi_{i-1/2}$ are upwinded from the previous cell $i-1$ or from a boundary condition; the terms at $x_{i+1/2}$ are linearly extrapolated, computed using the L and R basis moments, e.g., $\phi_{i+1/2}^+ = 2\langle\phi\rangle_R^+ - \langle\phi\rangle_L^+$. Because there are no derivatives of T in Eq. (8), there is no need to define T on the faces; the temperature has been assumed linear within a cell to relate T and T^4.

The choice of a LD spatial closure should preserve the equilibrium diffusion limit. In this limit, the MC HO solution will estimate angular consistency terms associated with an isotropic intensity, based on a spatially LD emission source. The isotropic-intensity consistency terms will produce LO equations that are equivalent to S_2 equations, with quadrature points of $\pm 1/2$. Because the spatial closure produces equations that are equivalent to an LDFE solution to these equations, we expect the equations to preserve the equilibrium diffusion limit [?, ?].

The linear-discontinuous (LD) closure with upwinding is not strictly positive. In particular, for optically thick cells with a steep intensity gradient, the solution becomes negative. These negative values of intensity can propagate to adjacent cells. In thick regions of TRT problems, reasonably fine spatial cells can still be on the order of millions of mean free paths; negative values with an LD representation are unavoidable in practice for such cells and mesh refinement is of minimal use. Typically, for a standard LDFE method, the equations are lumped to produce a strictly positive solution (for 1D) [?]. However, standard FE lumping procedures would introduce difficulties in computing the consistency terms from the HO solution. Thus, an alternative spatial closure is used that is equivalent to the standard FE lumping procedure. The L and R moments are defined the same as before, preserving the average within a cell, but the relation between the moments

28

and the outflow is modified. For example, for positive μ, the outflow is now defined as $\phi_{i+1/2}^+ = \langle\phi\rangle_R^+$. Because the basis function $b_{R,i}(x)$ is strictly positive, the outflow is positive. This closure is only used in cells where negative intensities occur.

0.8.4 Solving the Non-Linear LO System

We have used Newton's method to solve the global system of coupled LO equations, based on a typical linearization of the Planckian source with cross sections evaluated at temperatures of the previous iteration, as described in [**?**]. Once the system is linearized, a discrete matrix equation is formed. Isotropic scattering, including effective scattering terms from the linearization, are included in the system matrix. The system matrix is an asymmetric, banded matrix with a band width of seven and is inverted directly. Newton iterations are repeated until $\phi^{n+1}(x)$ and $T^{n+1}(x)$ are converged to a desired relative tolerance. Convergence is calculated using the spatial L_2 norm of the change in $\phi^{n+1}(x)$ and $T^{n+1}(x)$, relative to the norm of each solution. The lumping-equivalent discretization discussed above is used for cells where the solution for ϕ^{n+1} becomes negative. When negative values for $\phi^{n+1,\pm}(x)$ are detected, the lumping-equivalent discretization is used within those cells and that Newton step is repeated.

0.9 The ECMC High Order Solver

The transport equation to be solved by the HO solver is

$$\mu\frac{\partial I^{n+1,k+1/2}}{\partial x} + \left(\sigma_t^k + \frac{1}{c\Delta t}\right)I^{n+1,k+1/2} = \frac{\sigma_s}{2}\phi^{n+1,k} + \frac{1}{2}\left(\sigma_a^k acT^4\right)^{n+1,k} + \frac{\tilde{I}^n}{c\Delta t} \tag{21}$$

where the superscript k represents the outer HOLO iteration index. Material property indices will be suppressed from now on. Here, $k + 1/2$ denotes the ECMC solution within outer HOLO iteration k, whereas k and $k+1$ represent successive LO solves. The sources at k in Eq. (21) are estimated by the previous LO solution. Cross sections are evaluated at $T^{n+1,k}$. As all sources on the right side of the equation are known, this defines a fixed-source, pure absorber transport problem. We will solve this equation using ECMC. A more detailed description of the ECMC method can be found in [**?**], but

a brief overview is given here. A general proof of exponential convergence for related adaptive MC transport methods with a different formulation is depicted in [?].

In operator notation, Eq. (21) can be written as

$$\mathbf{L}^k I^{n+1,k+1/2} = q^k \tag{22}$$

where $I^{n+1,k+1/2}$ is the transport solution of the angular intensity based on the k-th LO estimate of q^k. The linear operator $\mathbf{L}^k$ is the continuous streaming plus removal operator defined by the left hand side of Eq. (7). The m-th approximate LDFE solution to Eq. (22) (m is the index of inner HO batches) is represented as $\tilde{I}^{n+1,(m)}$. The m-th residual is defined as $r^{(m)} = q - \mathbf{L}^k \tilde{I}^{n+1,(m)}$. For reference, the residual at iteration m in the HO solve is

$$r^{(m),k+1/2} = \frac{\sigma_s}{2} \phi^{n+1,k} + \frac{1}{2} \left(\sigma_a a c T^4 \right)^{n+1,k} + \frac{\tilde{I}^n}{c\Delta t} - \left(\mu \frac{\partial \tilde{I}^{n+1,k+1/2}}{\partial x} + \left(\sigma_t + \frac{1}{c\Delta t} \right) \tilde{I}^{n+1,k+1/2} \right)^{(m)} \tag{23}$$

where the k terms are LD in space on the coarsest mesh and are not recalculated at any point during the HO solve. The functional form of $\tilde{I}^n$ is defined from the final HO solution of the previous time step.

Addition of $\mathbf{L}I^{n+1} - q = 0$ to the residual equation and manipulation of the result yields the error equation

$$\mathbf{L}(I^{n+1} - \tilde{I}^{n+1,(m)}) = \mathbf{L}\epsilon^{(m)} = r^{(m)} \tag{24}$$

where I^{n+1} is the exact solution and $\epsilon^{(m)}$ is the true error in $\tilde{I}^{n+1,(m)}$. We have suppressed the HOLO iteration indices because the LO estimated q^k and $\mathbf{L}^k$ remain constant over the entire HO solve. The $\mathbf{L}$ operator in the above equation is inverted yielding the Monte Carlo LDFE projection of the error in $\tilde{I}^{n+1,(m)}$, i.e.,

$$\tilde{\epsilon}^{(m)} = \mathbf{L}^{-1} r^{(m)} \tag{25}$$

where $\mathbf{L}^{-1}$ is the Monte Carlo inversion of the streaming and removal operator. This inversion is strictly a standard Monte Carlo simulation. It is noted that the exact error in $\tilde{I}^{n+1,(m)}$ (with respect to Eq. (21)) is being estimated with MC; tallies produce a projection of the error onto a LDFE space-angle trial space. The space-angle moments of the error computed as $\tilde{\epsilon}^{(m)}$ can be added to the moments of $\tilde{I}^{n+1}(m)$ to produce a more accurate solution.

Here, we emphasize the solution $\tilde{I}^{n+1,(m)}$ represents the LDFE projection of the exact Monte Carlo solution to the transport problem defined by

Eq. (21). The discretization error is in q, i.e., the LD spatial representation of the emission and scattering source and the LDFE space-angle projection $\tilde{I}^n(x, \mu)$. The projection of the intensity is in general far more accurate than a standard finite element solution, e.g., a S_N collocation method in angle. In typical IMC calculations, the average energy deposition within a cell is computed using a standard path-length volumetric flux tally; the zeroth moment of the LDFE projection of ϵ is computed using an equivalent tally, preserving the zeroth moment of the true error.

Volumetric flux tallies over each space-angle element are required to estimate $\tilde{\epsilon}^{(m)}$. The LD approximation in space is used to relate the outflow within a cell to the volumetric moments, eliminating the need for face-averaged tallies. The procedure for representing the solution, sampling with negative and positive weight particles, and tally definitions are given in Appendix 0.16.

The ECMC algorithm is

1. Initialize the guess for $\tilde{I}^{n+1,(0)}$ to $\tilde{I}^n$ or the projection of $\tilde{I}^{n+1}$ from the latest HO solve

2. Compute $r^{(m)}$.

3. Perform a MC simulation to obtain $\tilde{\epsilon}^{(m)} = \mathbf{L}^{-1} r^{(m)}$

4. Compute a new estimate of the intensity $\tilde{I}^{n+1,(m+1)} = \tilde{I}^{n+1,(m)} + \tilde{\epsilon}^{(m)}$

5. Repeat steps 2 – 4 until desired convergence criteria is achieved.

The initial guess for the angular intensity $I^{n+1,(0)}$ is computed based on the previous solution for $\tilde{I}^n$. This is a critical step in the algorithm; it significantly reduces the required number of particles per time step because the intensity does not change drastically between time steps in optically-thick regions. It is noted that the ECMC batch (steps 1-4 of the algorithm) results in essentially the same estimate of the solution as the residual formulation used in [?]. The primary difference is that our method uses an LDFE trial space and iterates on the solution estimate by recomputing the residual.

Exponential convergence is obtained if the error ϵ is reduced each batch. With each batch, a better estimate of the solution is being used to compute the new residual, decreasing the magnitude of the MC residual source at each iteration m, relative to the solution I^{n+1}. Each MC estimate of the moments of ϵ still has a statistical uncertainty that is governed by the standard $1/\sqrt{N}$ convergence rate [?], for a particular source $r^{(m)}$, where N is the number

of histories performed. If the statistical estimate of the projection $\tilde{\epsilon}$ is not sufficiently accurate, then the iterations would diverge. It is noted that there is statistical correlation across batches because $I^{n+1,(m+1)}$ and $\epsilon^{(m)}$ are correlated through $I^{n+1,(m)}$ and the MC source $r^{(m)}$.

Because the exact angular intensity does not in general lie within the LDFE trial space, the iterative estimate of the error will eventually stagnate once the error cannot be sufficiently represented by a given FE mesh. An adaptive $h-$refinement algorithm has been implemented that can be used to allow the system to continue converging towards the exact solution [**?**, **?**]. For TRT problems where absorption-reemission physics dominate, the diffusive and slowly varying regions of the problem require a less refined angular mesh to capture the solution than typical neutronics problems. However, greater spatial resolution is needed due to steep spatial gradients. Once error stagnation has occurred (and mesh refinement has reached a maximum level), additional histories can be performed with a fixed residual source to estimate the remaining error in the current solution. Although the remaining error will converge statistically at a standard $1/\sqrt{N}$ convergence rate, the remaining error will be much smaller than for a standard MC simulation, producing a much more efficient solution method overall.

For the HO solver, in cells near the radiation wavefront, the LDFE trial space results in negative values in $\tilde{I}^{n+1}(x,\mu)$, similar to the LO solver. Because the residual formulation in ECMC allows for negative weight particles to occur, currently we do not treat these cells specially. We detect if the consistency terms lie in the appropriate half space at the end of the HO solve, an indication that the intensity was negative within that cell. If the terms are non-physical, then they are replaced with the corresponding S_2-equivalent value. In general, in such cells where the trial space cannot accurately represent the solution, error stagnation will rapidly occur.

0.9.1 Variance Reduction and Source Sampling

As in [**?**], because we are solving a pure absorber problem with Monte Carlo, we will allow particles to stream without absorption to reduce statistical variance in the tallies. The weight of particles is reduced deterministically along the path as they stream, with no need to sample a path length. Because particles are exponentially attenuated, the normalized weight is adjusted as $w(x,\mu) = w(x_0,\mu)\exp(-\sigma_t|(x - x_0)/\mu|)$, where x_0 is the starting location of the path. The tallies account for the continuously changing weight, as

given in Appendix 0.16. Histories are allowed to stream in this manner for 6 mean free paths (mfp)) before switching to analog path length sampling; this limits the tracking of very small weight histories. The choice of 6 mfp allows particles to continuously deposit weight until they reach 0.25% of their original weight. Path lengths are tracked in terms of mfp, so there is no need to resample at material interfaces.

As another way to improve efficiency, a modified systematic sampling method [**?**] was used for determining source particle locations. The goal is to effectively distribute particle histories to regions of importance, but to sample a sufficient number of histories in less probable regions to prevent large statistical noise. However, there is no need to sample histories in regions in thermal equilibrium. The residual gives a good indication of where histories are most likely to contribute to the error, particularly in optically thick cells where particles do not transport long distances. In the sampling algorithm the number of particle histories sampled in each space-angle cell is predetermined and proportional to the magnitude of the residual, including face and volumetric sources, within that cell. Then, for the predetermined number of histories within a cell, the source location is randomly sampled according to the residual source distribution of that cell. In cells where the relative magnitude of the residual is on the order of roundoff no particle histories are sampled. In these regions the problem is remaining in equilibrium and the solution is known exactly. For cells that are significant, but have a predetermined number of histories below some preset minimum N_{min}, the number of histories sampled in that cell is set to N_{min}. This is to limit bad statistics in low probability cells (this would be important for adaptively refined meshes). In the simulations performed for this work $N_{min} = 1$. This choice was made to keep the total number of histories per time step constant throughout the simulation for comparison to IMC.

0.10 COMPUTATIONAL RESULTS

We will compare results of the HOLO method to IMC with a source tilting algorithm for two test problems [**?**]. Also, we briefly compare performance in Section 0.10.3. For all IMC results, no local, discrete diffusion acceleration methods for effective scattering (e.g., those in [**?**, **?**]) are applied. Finally, we will demonstrate the efficiency advantage of ECMC in our HOLO algorithm by comparing the results to the same HOLO algorithm if the ECMC algo-

rithm is replaced with a standard Monte Carlo (SMC) simulation. Results are also given for the case of a single ECMC batch, which is similar to a RMC method.

A measure of variance in cell-averaged scalar intensities was calculated to provide a quantitative measure of the statistical accuracy of different solution methods. To form sample standard deviations, twenty independent simulations for each particular result were performed using unique random number generator seeds. The variance of a particular cell-averaged $\phi(x)$ is

$$S_i^2 = \frac{20}{20-1} \sum_{l=1}^{20} \left(\overline{\phi_i} - \phi_i^l \right)^2, \tag{26}$$

where ϕ_i^l is the cell-averaged scalar intensity for cell i from the l-th of 20 independent simulations and $\overline{\phi_i}$ is the corresponding sample mean from the 20 simulations. To provide a normalized, spatially-integrated result, we form a norm over cells as

$$\text{ß} = \left(\frac{\sum_{i=1}^{N_c} S_i^2}{\sum_{i=1}^{N_c} \overline{\phi_i}^2} \right)^{1/2}, \tag{27}$$

where N_c is the number of spatial cells.

We will also form a figure of merit (FOM) to demonstrate how statistical accuracy scales with the number of histories performed. Our FOM is defined as

$$\text{FOM} = \frac{1}{N_{\text{tot}} \text{ß}^2} \tag{28}$$

where N_{tot} is the total number of histories performed over the simulation. A larger value of the FOM indicates that the method produced less variance in the solution per history performed, for a given problem. This form of the FOM is typically chosen because the variance is expected to reduce inversely proportional to N_{tot}, so for standard MC simulations the FOM becomes, on average, independent of N_{tot} [?]. The FOM is not necessarily expected to be independent of N_{tot} for IMC or our HOLO method due to correlation of the solution between time steps; additionally, ECMC has correlations between batches.

0.10.1 Marshak Wave

For the first problem, the radiation and material energies are initially in equilibrium at 2.5×10^{-5} keV. An isotropic incident intensity of 0.150 keV is applied at $x = 0$; the incident intensity on the right boundary is 2.5×10^{-5} keV. The material properties are $\rho = 1$ g cm^{-3} and $c_v = 0.013784$ jks/keV-g. The absorption cross section varies as $\sigma(T) = 0.001 \; \rho \; T^{-3}$ (cm^{-1}). The simulation was advanced until $t = 5$ sh (1 sh $\equiv 10^{-8}$ s) with a fixed time step size of 0.001 sh. For comparison purposes, we have not used adaptive mesh refinement, only performed one HOLO iteration per time step, and use a fixed 3 HO batches with equal number of histories per batch. A relative tolerance of 10^{-6} for the change in $\phi(x)$ and $T(x)$ was used for the LO newton solver for all results. Radiation energy distributions are plotted as an equivalent temperature given by $T_r = (\phi/(ac))^{0.25}$. Cell-averaged quantities are plotted. Although isotropic scattering is handled by the LO solver in the algorithm described above, we have only considered problems with $\sigma_s = 0$ here. Results for neutronics with isotropic scattering included are given in [?].

Fig. 3a compares the cell-averaged radiation temperatures for the IMC and HOLO method with ECMC, for various number of spatial mesh cells N_c; we have used HOLO-ECMC to denote our algorithm because later results will use different HO solvers. For all IMC calculations, $n = 10^5$ histories per time step were used. For the HOLO method, we have used 4 equal-sized cells in μ for the finite-element angular mesh used by the ECMC solver. The spatial grid is the same for the HO and LO solvers. For the cases of $N_c = 25$ and $N_c = 200$, 4,000 histories per batch ($n = 12,000$ per time step) were used. For $N_c = 500$, 16,000 histories per time step were used due to increased number of space-angle cells that need to be sampled. The IMC and HOLO solutions agree as the mesh is converged. There is similar agreement in the location of the wavefront due to the linear shape of the emission source over a cell. The cells nearest the wavefront required use of the lumping-equivalent discretization and S_2 equivalent terms during the LO solve, resulting in strictly positive solutions.

Fig. 3b compares solutions for the case of 200 cells. For the IMC solution 10^5 histories per time step were simulated; for the HOLO method only 4,000 histories per batch (12,000 per time step) were simulated. There is significant statistical noise in the IMC solution compared to the HOLO solution. The HOLO solution visually demonstrates no statistical noise. Because the ECMC solve is only determining the change over the time step, the statisti-

cal noise in the result is small relative to the magnitude of I^{n+1}. Also, the source sampling only places particles in cells where the residual is large. No particles are sampled in the equilibrium region out front of the wave.

Table 1 compares ß and the FOM for IMC and the HOLO method, for different numbers of histories per time step. The FOM results are normalized to the value for IMC with $n = 12,000$. The HOLO method demonstrates less variance for the same numbers of histories, producing FOM values that are two orders of magnitude greater than for IMC. Where as the FOM remains relatively constant for IMC, as n is increased the FOM improves for the HOLO method. This is a result of each batch producing more statistically accurate estimates of the error ϵ, which results in an increased convergence rate of ϵ overall.

Table 1: **Comparison of sample statistics for the Marshak Wave problem. Simulation end time is t = 5 sh.**

	ß		FOM	
hists./step	IMC	HOLO-ECMC	IMC	HOLO-ECMC
12,000	3.40%	0.28%	1	145
100,000	1.22%	0.057%	0.93	422

0.10.2   Two Material Problem

This problem consists of an optically thin (left) and an optically thick (right) material region, with temperature-independent cross sections. The material properties are given in Table 2. Initially the radiation and material energies are in equilibrium at a temperature of 0.05 keV. An isotropic incident intensity of 0.500 keV is applied at $x = 0$ at $t = 0$; the isotropic incident intensity on the right boundary is 0.05 keV. The simulation end time is 5 sh. For all HOLO simulations, we have used 8 equal-sized mesh cells in μ. As for the Marshak problem, the cells nearest the wavefront required use of the lumping-equivalent discretization and S_2 equivalent terms during the LO solve.

Table 2: Material properties for two material problem

	$x \in [0, 0.5)$ cm	$x \in [0.5, 1.0]$ cm
σ_a (cm$^-1$)	0.2	2000
ρ (g cm$^-3$)	0.01	10.0
c_v (jks/keV-g)	0.1	0.1

Fig. 4a compares the HOLO and IMC radiation temperatures at the end of the simulation. The IMC and HOLO results show good agreement over the finer mesh. On the coarse mesh ($N_c = 20$), the LDFE representation of T^4 in the HOLO method predicts the location of the wavefront more accurately than the IMC method with source tilting.

Fig. 4b demonstrates the benefit of ECMC as a HO solver compared to standard MC. The HOLO algorithm with the ECMC HO solver (HOLO-ECMC) results are for running 3 batches of 10,000 histories, per time step. The solution for the HOLO method with a standard MC solver as the HO solver (HOLO-SMC) with standard source sampling uses 10^5 histories per time step. The HOLO-SMC solution demonstrates significant statistical noise. This noise is introduced into the LO solver by bad statistics in computing the consistency terms. Also plotted is an S$_2$ solution obtained with consistency terms that are equivalent to S$_2$ and no HO correction. The S$_2$ solution results in an artificially fast wavefront, as expected, demonstrating the necessity of HO correction in this problem.

Table 3 compares the FOM and ß for IMC and the HOLO-ECMC method. The FOM values are normalized to the value for IMC with $n = 30,000$. The end time was reduced to 2 sh for these results to reduce computational times. The reduction in variance by the HOLO method over IMC is substantial. The improvement of the FOM for the HOLO method compared to IMC is greater than for the Marshak wave problem. This improvement is because the wave moves much slower in right region of this problem, due to the large, constant cross section. Also, in the optically thin region of the problem the solution quickly comes to equilibrium. Thus, the ECMC algorithm has to estimate a very small change in the intensity over a time step. Additionally, difficulties in resolving the solution at the wavefront are not as severe compared to the Marshak wave problem, where the cold cells have a much larger cross section.

Table 3: **Comparison of sample statistics for the two material problem for 200 x cells. Simulation end time is t = 2 sh.**

hists./step	ß		s_{max}	
	IMC	HOLO-ECMC	IMC	HOLO-ECMC
30,000	3.63%	0.01%	1	104,000
100,000	1.96%	0.003%	1.03	360,000

0.10.3 Performance comparison of IMC and HOLO-ECMC

We have measured the total CPU time for simulations to provide a simplified measure of the computational cost. These results compare how computational times change the two different problems and how the methods scale with time step size and particle histories. Absolute comparisons in the computational cost of the two methods cannot be made because the methods are implemented in different code infrastructures. Additionally, the HOLO method fully resolves non-linearities at each time step, whereas IMC is using a single linearized step with lagged cross sections. Simulations were performed on the same processor, using a single CPU core. Reported times are the average of 10 runs and all results used 200 x cells, $\Delta t = 0.001$ sh, and an end time of $t = 2$ sh.

Table 4 compares the average simulation time per history performed for the Marshak wave problem. The average time per history is computed by dividing the total simulation time by the total number of histories performed (e.g., the time of the LO solves is included for the HOLO method). Results are given for different numbers of histories per time step, as well as a case with an increased time step size. The table also includes the number of LO iterations performed per LO solve for the HOLO method, averaged over all time steps; there are two LO solves per time step. The same results are reported for the two material problem in Table 5.

The HOLO method does not scale with the number of histories due to the fixed cost of the LO solver. The cost of the LO solver is more significant at the lower history counts compared to the case of 10^5 histories, for both problems. There is a slight increase in the number of newton iterations as the time step is increased, but the average cost per history is not significantly increased. Similar to the results in [**?**], as the time step size is increased to to 0.005 sh, the IMC method increases in cost per time step, due to

38

an increase in effective scattering events, particularly for the two material problem. Because the cross sections in the the two material problem do not have a T^{-3} behavior, the cost of the effective scattering cross section in IMC is more apparent, resulting in longer simulation times.

Table 4: **Comparison of average CPU times per history and LO iteration counts for the Marshak Wave problem.**

hists./step	$\Delta t(sh)$	IMC (μs/hist.)	HOLO-ECMC (μs/hist)	Newton iters./LO solve
100,000	0.001	10	5.3	3.8
12,000	0.001	9.7	8.1	4.1
12,000	0.005	19	9.4	6.2

Table 5: **Average CPU times per history and LO iteration counts required for the two material problem.**

hists./step	$\Delta t(sh)$	IMC (μs/hist.)	HOLO-ECMC (μs/hist)	Newton iters./LO Solve
100,000	0.001	17	3.5	4.9
30,000	0.001	18	6.9	5.0
30,000	0.005	59	7.4	7.6

0.10.4   Comparison of different HO Solvers

In this section we compare the results of our HOLO algorithm with different HO solvers for the test problems in Section 0.10.1 and 0.10.2. We compare standard MC (SMC) as a HO solver to the HOLO algorithm with ECMC using both three batches and a single batch, per time step. The use of a single batch is similar to the approach in [**?**]. Results are tabulated for 200 x cells, using the same total number of histories per time step, divided evenly among the batches.

Tables 6 and 7 compare the results for the Marshak wave and two material problems. The number of batches for each ECMC case is indicated in parenthesis. The FOM values are normalized to the reference IMC result for the corresponding problem. For HOLO-SMC there is minimal reduction in variance compared to IMC in the Marshak wave problem, and the two material problem actually demonstrates worse variance. Sufficient histories are not performed to accurately estimate consistency terms throughout the

problem. For ECMC, a single batch produces less variance than the case of three equal batches. This indicates that if the solution cannot be resolved with the trial space (i.e., the intensity is driven negative), a single large batch may be more accurate. It is noted that these results only account for statistical variance, and do not account for accuracy, which will depend on the estimates of ϵ computed each iteration.

Table 6: **Comparison of sample statistics for the Marshak Wave problem. Number of ECMC batches is indicated in parenthesis.**

	ß			FOM		
hists./step	SMC	ECMC (1)	ECMC (3)	SMC	ECMC (1)	ECMC (3)
12,000	2.77%	0.10%	0.28%	1.50	1280	145
100,000	0.98%	0.03%	0.06%	1.43	1270	422

Table 7: **Comparison of sample standard deviations for the two material problem. Number of ECMC batches is indicated in parenthesis.**

	ß			FOM		
hists./step	SMC	ECMC (1)	ECMC (3)	SMC	ECMC (1)	ECMC (3)
30,000	5.35%	0.002953%	0.011%	0.46	1.51×10^6	1.04×10^4
100,000	2.85%	0.001474%	0.0033%	0.49	1.80×10^6	3.59×10^4

0.10.5 Pre-heated Marshak wave problem and adaptive mesh refinement

Finally, to demonstrate the potential of ECMC with adaptive space-angle mesh refinement, we perform results for a modified Marshak wave problem. The problem is modified so that the LDFE trial space can accurately represent the solution (i.e., the intensity is strictly positive). Mesh refinement is of minimal use in the previous problems due to most of the error existing at the wavefronts, caused by the large cross sections. The modified problem has the same material properties and left boundary source as the Marshak wave problem in Section 0.10.1. However, the initial equilibrium temperature and right boundary condition are raised to 0.03 keV. The higher initial temperature reduces the initial cross section and increases the strength of the emission source within cells. The LDFE mesh can now sufficiently resolve

the solution and lumping is not required by the LO solution. The simulation end time is 0.5 sh with a constant time step of $\Delta t = 0.001$ sh.

Fig. 5 compares the result from HOLO-ECMC with three batches and IMC. It was found that 100 x cells was sufficient to resolve the solution spatially. There is slightly more noise in IMC past the wavefront due to the increased emission source. Additionally, the opacity is thin enough that some photon energy is able to reach the right boundary, in front of the wavefront.

Table 8 compares the variances for this problem for the various HO solvers. The FOM values are normalized to the case of HOLO-SMC with 12,000 histories per time step. The final row of the table is for an ECMC simulation with adaptive mesh refinement (AMR). The strategy for refinement is described in Appendix 0.17. The adaptive mesh refinement case used a total of nine batches, with a refinement occurring at the end of the third and sixth batches, for every time step. The initial number of histories was adjusted so that the average number of histories per time step is near 100,000; on average 99,881 histories per time step were used. All ECMC meshes used 4 equally-spaced μ cells initially. The improvement in variance by ECMC compared to SMC is not as significant as for the other problems. This is a result of the reduced opacity leading to intensity changing throughout the spatial and angular domains. The FOM is highest for the case of ECMC with adaptive refinement. When the solution can be resolved, the adaptive algorithm allows for a higher convergence rate of statistical variance. It is noted that the consistency terms and LO solution are still computed over the fixed, coarser mesh. However, in general, the refined mesh can produce higher accuracy in consistency terms that is not being measured by the FOM.

Table 8: **Comparison of sample statistics for the pre-heated marshak wave problem for 100 x cells. Number of ECMC batches is indicated in parenthesis.**

	ß			FOM		
hists./step	SMC	ECMC (1)	ECMC (3)	SMC	ECMC (1)	ECMC (3)
12,000	0.86%	0.13%	0.24%	1	41	13
100,000	0.16%	0.042%	0.08%	3.32	52	15
99,881 (AMR, 9 batches)	–	0.038%		–	61	

0.11 CONCLUSIONS

We have been able to produce solutions for Marshak wave test problems using a new HOLO method that are in agreement with IMC. Unlike IMC, our method requires no effective scattering events to be included in the MC simulation, which limits the run time of particle tracking, while adding the cost of a LO newton solver. Average LO iteration counts did not significantly increase as the time step size was increased. The LDFE spatial representation mitigates issues with teleportation error, producing results with spatial accuracy comparable to IMC with source tilting. The ECMC approach, with initial guesses based on the previous radiation intensity, results in efficient reduction of statistical error and allows for particles to be distributed to largely varying regions of the problem. The LO solver resolves the non-linearities in the equations resulting in a fully implicit time discretization. The LO solver can accurately and efficiently resolve the solution in diffusive regions, while the HO transport solver provides the accuracy of a full transport treatment where necessary.

The primary difficulty to overcome in the ECMC algorithm is when the solution cannot be accurately represented by the trial space, e.g., in optically thick cells where the solution is driven negative. We are currently developing an approach to allow the ECMC iterations to continue converging globally when there are such regions present. It is necessary to ensure the closure in the LO system is consistent with the HO representation for the solution in such regions. The ability to represent the solution accurately in rapidly varying regions of the problem will be key for generalization of this method to higher dimensions. A formulization of the ECMC method that allows for time-continuous MC transport (similar to IMC) is also currently being investigated. This may reduce some of the loss of accuracy in optically thin regions due to the time discretization of the transport equation in the HO solver. However, greater time accuracy is not of primary concern as this method is intended for use in problems dominated by large absorption opacities, where the LO acceleration is critical. Inclusion of Compton scattering in this algorithm, which would introduce additional non-linear dependence through energy exchange with the material, is a topic for future research.

Future work will also explore the accuracy of the HOLO method, in particular, analyzing the optimal number of batches and the benefit of adaptive refinement. This will likely require the use of manufactured solutions. The sensitivity of the method to mesh sizes and time step sizes will be in-

vestigated more thoroughly. Ultimately, we plan to extend this method to multiple spatial dimensions for the case of multigroup TRT equations. For TRT problems, it is important that the LO spatial discretization satisfies the equilibirium diffusion limit. To extend to higher dimensions, our LDFE representation may require the use of a higher-degree spatial representation for the LO system to achieve the diffusion limit. Further asymptotic analysis on the method will be applied before implementation. It may be necessary to use a different LO system (e.g., the non-linear diffusion acceleration approach in [?]), if the S_2-like equations become too inefficient or difficult to implement in higher dimensions. Alternatively, a variable Eddington Tensor approach may provide more stability in rapidly variable regions of the problem while still allowing for a consistent, LDFE solution that is efficiently solvable.

ACKNOWLEDGEMENTS

0.12   Diffusion Synthetic Acceleration

To accelerate source iteration in the LO system, a version of WLA DSA is used. The following derivations are to solve a diffusion equation which can be used to compute the source iteration error in the LO sweeps.

0.12.1   Forming a Continuous Diffusion Equation

Beginning with the P_1 equations for a steady-state problem

$$\frac{\partial J}{\partial x} + \sigma_a \phi = Q \tag{29}$$

$$\sigma_t J + \frac{1}{3}\frac{\partial \phi}{\partial x} = 0 \tag{30}$$

$$\tag{31}$$

spatial finite element moments are taken. The spatial moments are defined as

$$\langle \cdot \rangle_L = \frac{2}{h_i} \int_{x_{i-1/2}}^{x_{i+1/2}} \mathrm{d}x \, b_{L,i}(x) \, (\cdot) \tag{32}$$

$$\langle \cdot \rangle_R = \frac{2}{h_i} \int_{x_{i-1/2}}^{x_{i+1/2}} \mathrm{d}x \, b_{R,i}(x) \, (\cdot). \tag{33}$$

where $b_{L,i}(x) = (x_{i+1/2} - x)/h_i$ and $b_{R,i}(x) = (x - x_{i-1/2})/h_i$. The scalar flux ϕ will ultimately be assumed continuous at faces. The scalar flux is assumed linear on the interior of the cell, i.e., $\phi(x) = \phi_L b_L(x) + \phi_R b_R(x)$, for $x \in (x_{i-1/2}, x_{i+1/2})$. Taking the left moment, evaluating integrals, and rearranging yields

$$J_i - J_{i-1/2} + \frac{\sigma_{a,i} h_i}{2} \left(\frac{2}{3} \phi_{L,i} + \frac{1}{3} \phi_{R,i} \right) = \frac{h_i}{2} \langle q \rangle_{L,i} \,, \tag{34}$$

where J_i is the average of the current over the cell. The moments of q are not simplified to be compatible with the LO moment equations. For the R moment

$$J_{i+1/2} - J_i + \frac{\sigma_{a,i} h_i}{2} \left(\frac{2}{3} \phi_{L,i} + \frac{1}{3} \phi_{R,i} \right) = \frac{h_i}{2} \langle q \rangle_{R,i} \,. \tag{35}$$

The equation for the L moment is evaluated for cell $i + 1$ and added to the R moment equation evaluated at i. The current is assumed continuous at $i + 1/2$ to eliminate the face current from the system. The sum of the two equations becomes

$$J_{i+1} - J_i + \frac{\sigma_{a,i+1} h_{i+1}}{2} \left(\frac{2}{3} \phi_{L,i+1} + \frac{1}{3} \phi_{R,i+1} \right) + \frac{\sigma_{a,i} h_i}{2} \left(\frac{1}{3} \phi_{L,i} + \frac{2}{3} \phi_{R,i} \right) =$$
$$\frac{h}{2} \left(\langle q \rangle_{L,i+1} + \langle q \rangle_{R,i} \right). \tag{36}$$

The scalar flux is assumed continuous at each face, i.e., $\phi_{L,i+1} = \phi_{R,i} \equiv \phi_{i+1/2}$. We then approximate the cell-averaged currents with Fick's law as

$$J_i = -D_i \frac{\phi_{i+1/2} - \phi_{i-1/2}}{h_i}. \tag{37}$$

Combining the definition and rearranging yields the following discrete diffusion equation:

$$\left(\frac{\sigma_{a,i+1}h_{i+1}}{6} - \frac{D_{i+1}}{h_{i+1}}\right)\phi_{i+3/2} + \left(\frac{D_{i+1}}{h_{i+1}} + \frac{D_i}{h_i} + \frac{\sigma_{a,i+1}h_{i+1}}{3} + \frac{\sigma_{a,i}h_i}{3}\right)\phi_{i+1/2}$$
$$+ \left(\frac{\sigma_{a,i}h_i}{6} - \frac{D_i}{h_i}\right)\phi_{i-1/2} = \frac{h_{i+1}}{2}\langle q\rangle_{L,i+1} + \frac{h_i}{2}\langle q\rangle_{R,i} \ . \quad (38)$$

This system can be solved to get ϕ at each face. To allow for the use of lumped or standard LD in these equations, we introduce the factor θ, with $\theta = 1/3$ for standard LD, and $\theta = 1$ for lumped LD. The diffusion equation becomes

$$\left(\frac{\sigma_{a,i+1}h_{i+1}}{4}(1-\theta) - \frac{D_{i+1}}{h_{i+1}}\right)\phi_{i+3/2} + \left(\frac{D_{i+1}}{h_{i+1}} + \frac{D_i}{h_i} + \left(\frac{1+\theta}{2}\right)\left[\frac{\sigma_{a,i+1}h_{i+1}}{2} + \frac{\sigma_{a,i}h_i}{2}\right]\right)\phi_{i+1/2}$$
$$+ \left(\frac{\sigma_{a,i}h_i}{4}(1-\theta) - \frac{D_i}{h_i}\right)\phi_{i-1/2} = \frac{h_{i+1}}{2}\langle q\rangle_{L,i+1} + \frac{h_i}{2}\langle q\rangle_{R,i} \ . \quad (39)$$

Boundary Conditions

The LO system exactly satisfies the inflow boundary conditions, therefore we choose a vacuum boundary condition for the left-most cell. The equation for the left moment at the first cell is given by

$$J_1 - J_{1/2} + \frac{\sigma_{a,i}h_i}{2}\left(\frac{1+\theta}{2}\phi_{L,i} + \frac{1-\theta}{2}\phi_{R,i}\right) = \frac{h_i}{2}\langle q\rangle_{L,i} \ , \quad (40)$$

The Marshak boundary condition for the vacuum inflow at face $x_{1/2}$ is given as

$$J_{1/2}^+ = 0 = \frac{\phi_{1/2}}{4} + \frac{J_{1/2}}{2}, \quad (41)$$

which can be solved for $J_{1/2}$. Substitution of the above equation and Eq. (37) into Eq. (40) gives

$$\left(\frac{1}{2} + \sigma_{a,1}h_1\frac{1+\theta}{4} - \frac{D_1}{h_1}\right)\phi_{1/2} + \left(\sigma_{a,1}h_1\frac{1-\theta}{4} - \frac{D_1}{h_1}\right)\phi_{3/2} = \frac{h_i}{2}\langle q\rangle_{L,1} \quad (42)$$

a similar expression can be derived for the last cell.

0.12.2 Mapping Solution onto LD Unknowns

Solution of the continuous diffusion equation in the previous section provides correction values for ϕ on the faces, denoted as $\phi_{i+1/2}^C$. We now need to determine the correction these results provide for the LD representation of ϕ. To do this, first we take the L and R finite element moments of the P_1 equations. A LDFE dependence is assumed on the interior of the cell for J and ϕ. Taking moments of Eq. (29) and simplifying yields

$$J_{i+1/2} - \frac{J_{L,i} + J_{R,i}}{2} + \frac{\sigma_{a,i} h_i}{2} \left(\frac{1}{3} \phi_{L,i} + \frac{2}{3} \phi_{R,i} \right) = \frac{h_i}{2} \langle q \rangle_{R,i} \qquad (43)$$

$$\frac{J_{L,i} + J_{R,i}}{2} - J_{i-1/2} + \frac{\sigma_{a,i} h_i}{2} \left(\frac{2}{3} \phi_{L,i} + \frac{1}{3} \phi_{R,i} \right) = \frac{h_i}{2} \langle q \rangle_{L,i} \qquad (44)$$

The moment equations for Eq. (30) are

$$\frac{1}{3} \left(\phi_{i+1/2} - \frac{\phi_{i,L} + \phi_{i,R}}{2} \right) + \frac{\sigma_{t,i} h_i}{2} \left(\frac{1}{3} J_{L,i} + \frac{2}{3} J_{R,i} \right) = 0 \qquad (45)$$

$$\frac{1}{3} \left(\frac{\phi_{i,L} + \phi_{i,R}}{2} - \phi_{i-1/2} \right) + \frac{\sigma_{t,i} h_i}{2} \left(\frac{2}{3} J_{L,i} + \frac{1}{3} J_{R,i} \right) = 0 \qquad (46)$$

Using similar equation for all the inflow currents, the balance equations for ϕ become The face terms $J_{i\pm1/2}$ and $\phi_{i\pm1/2}$ need to be eliminated from the system. The scalar flux is assumed to be the value provided by the continuous diffusion solution at each face, i.e., $\phi_{i\pm1/2} = \phi_{i\pm1/2}^C$. The currents are decomposed into half-range values to decouple the equations between cells. At $x_{i+1/2}$, the current is composed as $J_{i+1/2} = J_{i+1/2}^+ - J_{i+1/2}^-$, where $+$ and $-$ denote the positive and negative half ranges of μ, respectively. Typically, the incoming current $J_{i+1/2}^-$ is upwinded from cell $i+1$. However, we approximate the incoming current based on $\phi_{i+1/2}^C$. The P_1 approximation provides the following relation

$$\phi = 2(J^+ + J^-). \qquad (47)$$

At $x_{i+1/2}$, the above expression is solved for the incoming current $J_{i+1/2}^-$. The total current becomes, with $\phi_{i+1/2} = \phi_{i+1/2}^C$,

$$J_{i+1/2} = J_{i+1/2}^+ - J_{i+1/2}^- = 2 J_{i+1/2}^+ - \frac{\phi_{i+1/2}^C}{2}, \qquad (48)$$

46

In the positive direction, at the right face, the values of ϕ and J are based on the LD representation within the cell at that face, i.e., $\phi_{R,i}$ and $J_{R,i}$. The standard P_1 approximation for the half-range currents and fluxes are used[?], i.e.,

$$J^{\pm} = \frac{\gamma\phi}{2} \pm \frac{J}{2}, \tag{49}$$

where γ accounts for the difference between the LO parameters and the true P_1 approximation. Thus, for the right face and positive half-range,

$$J^{+}_{i+1/2} = \frac{\gamma}{2}\phi_{i,R} + \frac{J_{i,R}}{2} \tag{50}$$

A similar expression can be derived for $x_{i-1/2}$. The total currents at each face are thus

$$J_{i+1/2} = \gamma\phi_{i,R} + J_{i,R} - \frac{\phi^C_{i+1/2}}{2} \tag{51}$$

$$J_{i-1/2} = \frac{\phi^C_{i-1/2}}{2} - \gamma\phi_{i,L} + J_{i,L} \tag{52}$$

Substitution of these results back into the LD balance equations and introduction of the lumping notation yields the final equations

$$\left(\gamma\phi_{i,R} + J_{i,R} - \frac{\phi^C_{i+1/2}}{2}\right) - \frac{J_{L,i} + J_{R,i}}{2} + \frac{\sigma_{a,i}h_i}{2}\left(\frac{(1-\theta)}{2}\phi_{L,i} + \frac{(1+\theta)}{2}\phi_{R,i}\right) = \frac{h_i}{2}\langle q\rangle_{R,i} \tag{53}$$

$$\frac{J_{L,i} + J_{R,i}}{2} - \left(\frac{\phi^C_{i-1/2}}{2} - \gamma\phi_{i,L} + J_{i,L}\right) + \frac{\sigma_{a,i}h_i}{2}\left(\frac{(1+\theta)}{2}\phi_{L,i} + \frac{(1-\theta)}{2}\phi_{R,i}\right) = \frac{h_i}{2}\langle q\rangle_{L,i} \tag{54}$$

$$\frac{1}{3}\left(\phi^C_{i+1/2} - \frac{\phi_{i,L} + \phi_{i,R}}{2}\right) + \frac{\sigma_{t,i}h_i}{2}\left(\frac{(1-\theta)}{2}J_{L,i} + \frac{(1+\theta)}{2}J_{R,i}\right) = 0 \tag{55}$$

$$\frac{1}{3}\left(\frac{\phi_{i,L} + \phi_{i,R}}{2} - \phi^C_{i-1/2}\right) + \frac{\sigma_{t,i}h_i}{2}\left(\frac{(1+\theta)}{2}J_{L,i} + \frac{(1-\theta)}{2}J_{R,i}\right) = 0. \tag{56}$$

The above equations are completely local to each cell and fully defined. The system can be solved for the the desired unknowns $\phi_{i,L}$, $\phi_{i,R}$, $J_{i,L}$, and $J_{i,R}$.

0.12.3 DSA Source Definition

The above discretization procedure is used to determine the error in the scalar flux. The sources $\langle q \rangle_{L/R}$ thus need to be defined. They are simply the residual in the scattering iterations, given by

$$q = \sigma_s \left(\phi^{l+1/2} - \phi^l \right). \tag{57}$$

The spatial moments are straight forward:

$$\langle q \rangle_{L,i} = \sigma_{s,i} \left(\langle \phi^{l+1/2} \rangle_{L,i} - \langle \phi^l \rangle_{L,i} \right) \tag{58}$$

The above equation is valid for lumping or standard LD. This is because the LO moments are defined differently for LLD or LD, resulting in equations that are consistent. For instance, for lumped LD, the LO system uses the spatial closure that the edge value is defined as the moment, i.e., $\langle \phi \rangle_{R,i} \equiv \phi_{R,i}$. For a standard lumped source, we desire the right equation to have $\langle q \rangle_{R,i} = \sigma_s(\phi_{R,i}^{l+1/2} - \phi_{R,i}^l)$. Substituting the lumped closure into the right hand side of this equation gives back the original equation, i.e., $\langle q \rangle_{R,i} = \sigma_{s,i} \left(\langle \phi^{l+1/2} \rangle_{R,i} - \langle \phi^l \rangle_{R,i} \right)$. The same is true for standard LD.

0.12.4 Updating the LO Unkowns

We now have a correction to J and ϕ for the volumetric finite element unknowns. Because we are interested in the time-dependent solution, we need to accelerate the solution for the half-range fluxes, rather than just the scalar flux. We only accelerate the zeroth moment of the angular intensity. The error in the scalar intensities are defined as

$$\delta \phi^{\pm} = \frac{\delta \phi}{2} \pm \frac{3 \delta J}{4} \tag{59}$$

Spatial moments are taken of $\delta \phi^{\pm}$, using the lumping notation of LD on the interior

$$\langle \delta \phi^{\pm} \rangle_L = \frac{1+\theta}{2} \delta \phi_L^{\pm} + \frac{1-\theta}{2} \delta \phi_R^{\pm} \tag{60}$$

$$\langle \delta \phi^{\pm} \rangle_R = \frac{1-\theta}{2} \delta \phi_L^{\pm} + \frac{1+\theta}{2} \delta \phi_R^{\pm}, \tag{61}$$

where Eq. (59) can be used to get in terms of $\delta \phi_{L/R}$ and $\delta J_{L/R}$. It is noted that for consistency, the updates to the moments depend on the lumping notation, even though the sources are defined the same in both cases.

0.13 Analytic Neutronics answer for Source fixup

In this section we model a fixed-source, pure-absorber neutronics calculation where we know the analytic answer to test our fixup. If we make the mesh thick enough, we can set the solution to be the equilibrium answer $\psi(x) = \frac{q(x)}{2\sigma_a}$. For a general isotropic source $Q(x)$, the 1D transport equation to be solved is

$$\mu\frac{\partial\psi}{\partial x} + \sigma_a\psi(x,\mu) = \frac{q(x)}{2} \tag{62}$$

with boundary condition $\psi(0,\mu) = \psi_{inc}$, $\mu > 0$ and $\psi(x_R,\mu) = \frac{q(x_R)}{2\sigma_a}$ for $\mu < 0$, where x_R is the right boundary. This first order differential equation is solved using an integration factor. The solution to this equation for $\mu > 0$ is given by

$$\psi(x,\mu) = \psi_{inc}e^{\frac{-\sigma_a x}{\mu}} + \int_0^x \frac{q(x')}{2\mu}e^{\frac{-\sigma_a x'}{\mu}}\,\mathrm{d}x', \quad \mu > 0 \tag{63}$$

Integration of this result over the positive half range of μ gives

$$\phi^+(x) = \psi_{inc}\,\mathrm{E}_2(\sigma_a x) + \frac{1}{2}\int_0^x q(x')\,\mathrm{E}_1(\sigma_a x')\mathrm{d}x'. \tag{64}$$

In the simplification of a constant source, the integral reduces to

$$\phi^+(x) = \psi_{inc}\,\mathrm{E}_2(\sigma_a x) + \frac{q}{2\sigma_a}\left(1 - \mathrm{E}_2(\sigma_a x)\right). \tag{65}$$

Also, for a constant source the solution for the negative half range becomes a constant, i.e.,

$$\phi^-(x) = \frac{q}{\sigma_a} \tag{66}$$

Combination of the above two equations gives the solution for the scalar flux:

$$\phi(x) = \psi_{inc}\,\mathrm{E}_2(\sigma_a x) + \frac{q}{2\sigma_a}\left(1 - \mathrm{E}_2(\sigma_a x)\right) + \frac{q}{\sigma_a}. \tag{67}$$

0.14 Face Tallies and correction near $\mu = 0$

Face-averaged estimators of the angular error are required to compute the outflow for estimating the spatial closure. The standard face-based tallies [?, ?] are used. Tallies are weighted by the appropriate basis functions

to compute a linear FE projection in μ at each face. The tally score, for the angular-averaged error $\epsilon_{a,i}$ is defined as

$$\hat{\epsilon}_{a,i\pm1/2,j} = \frac{1}{N} \sum_{m=1}^{N_{i\pm1/2,j}} \frac{w_m(x_{i\pm1/2}, \mu)}{h_\mu |\mu|}, \tag{68}$$

where N is the number of histories performed and $N_{i\pm1/2,j}$ is the number of histories that crossed the surface $i \pm 1/2$, in the j angular element. For the first moment, the tally is

$$\hat{\epsilon}_{\mu,i\pm1/2,j} = \frac{1}{N} \sum_{m=1}^{N_{i+1/2,j}} 6 \left(\frac{\mu - \mu_j}{h_\mu} \right) \frac{w_m(x_{i\pm1/2}, \mu)}{|\mu| h_\mu}. \tag{69}$$

For positive and negative direction outflows are tallied on the $x_{i+1/2}$ and $x_{i-1/2}$ faces, respectively. Particles are only tallied after leaving a cell, and, as discussed in Section 0.15, particles born on a surface do not contribute to the tally of that surface.

Near $\mu = 0$, particles can contribute large scores to the zeroth angular moment that lead to large and unbounded variances [?]. To avoid large variances, we have applied the standard fixup [?, ?]. For $|\mu|$ below some small value μ_{cut}, particles contribute the expected score over the range $(0, |\mu_{cut}|)$, based on an approximate, isotropic particle density. Thus, scores in this range have no variance. Assuming an isotropic particle density I_0, the average of $1/\mu$, for positive μ, is

$$\overline{1/\mu} = \frac{\int_0^{\mu_{cut}} \frac{1}{\mu} I_0 \, \mathrm{d}\mu}{\int_0^{\mu_{cut}} I_0 \, \mathrm{d}\mu} = \frac{2}{\mu_{cut}}. \tag{70}$$

For negative μ, $\overline{1/\mu} = -2/\mu_{cut}$. All particles in the range $(0, |\mu_{cut}|)$ contribute the expected score by evaluating the tallies at $\pm\mu = \pm2/\mu_{cut}$. It is noted that the first moment of μ can be estimated without this correction by only applying the correction to the constant weighted in Eq. (69). However, this would be inconsistent with the zeroth moment tally. Additionally, assuming an isotropic intensity over the range helps to limit the first moment near $\mu = 0$, which the LD trial space generally cannot resolve anyways, as discussed in ???.

0.15 MC solution with LDD trial space

The inclusion of the outflow discontinuity has a minimal effect on the treatment of the residual source. The residual source and process of estimating moments of the error on the interior of a space-angle cell is unchanged. The process of estimating the solution on the outgoing face requires tallying the solution when particles leave a cell. The tallying process is discussed later in Section 0.14.

Applying L to the LDD trial space, as shown in Fig. ??, results in two δ functions at each interior face. For positive flow, at a face $x_{i+1/2}$, the face portion of the residual is defined as

$$r_{\text{face}}(x_{i+1/2}) = -\mu \frac{\partial \tilde{I}^{(m)}}{\partial x}\Big|_{x_{i+1/2}} \tag{71}$$

$$= r_{\text{face}}(x^-_{i+1/2})\delta^-(x - x_{i+1/2}) + r_{\text{face}}(x^+_{i+1/2})\delta^+(x - x_{i+1/2}) \tag{72}$$

where

$$r_{\text{face}}(x^-_{i+1/2}) = -\mu\left(\tilde{I}^{(m)}(x_{i+1/2}, \mu) - \tilde{I}^{(m)}(x^-_{i+1/2}, \mu)\right) \tag{73}$$

$$r_{\text{face}}(x^+_{i+1/2}) = -\mu\left(\tilde{I}^{(m)}(x^+_{i+1/2}, \mu) - \tilde{I}^{(m)}(x_{i+1/2}, \mu)\right). \tag{74}$$

Here, $I^{(m)}(x^+_{i+1/2})$ and $I^{(m)}(x^-_{i+1/2})$ are the LD solution extrapolated to $x_{i+1/2}$ from the x cell i and cell $i+1$, respectively. Particles sampled from the two δ-functions have the same starting location. The only difference is, for positive μ, particles sampled from $r_{\text{face}}(x^-_{i+1/2})$ will contribute to the face tally at $x_{i+1/2}$; the opposite is true for negative μ.

To reduce variance, we do not sample the two δ functions independently. Instead, we combine the two δ-functions into a single face source, do not score particles at the face from which they are sampled. To account for the untallied error, we add the analytic contribution to the error from the face source to the corresponding face at the end of a batch. It is noted the combination of the two δ-functions produces the same residual source as the original LD residual.

Define the additional error contribution from the face sources at $x_{i+1/2}$ as $\delta\epsilon^{(m)}$. This additional error is tallied everywhere by MC, except for at $x_{i+1/2}$. The transport equation satisfied by $\delta\epsilon^{(m)}$, for positive μ, with effective total

cross section $\hat{\sigma}_t$, is

$$\mu \frac{\partial \delta \epsilon^{(m)}}{\partial x} + \hat{\sigma}_t \delta \epsilon^{(m)} = r_{\text{face}}(x_{i+1/2}^-)\delta^-(x - x_{i+1/2}) + r_{\text{face}}(x_{i+1/2}^+)\delta^+(x - x_{i+1/2})$$
(75)

This equation is integrated from $x_{i+1/2} - \alpha$ to $x_{i+1/2}$ to produce

$$\mu \delta \epsilon^{(m)}(x_{i+1/2}, \mu) - \mu \delta \epsilon^{(m)}(x_{i+1/2} - \alpha, \mu) + \int_{x_{i+1/2}-\alpha}^{0} \hat{\sigma}_t \delta \epsilon^{(m)} \mathrm{d}x$$

$$= r_{\text{face}}(x_{i+1/2}^-) + \int_{x_{i+1/2}-\alpha}^{0} r_{\text{face}}(x_{i+1/2}^+)\delta^+(x - x_{i+1/2})\mathrm{d}x. \quad (76)$$

The integral on the right side of the equation is zero because $\delta^+(x - x_{i+1/2})$ is zero for $(-\infty, x_{i+1/2}]$. The limit of the above equation is taken as $\alpha \to 0$, i.e.,

$$\lim_{\alpha \to 0} \left(\mu \delta \epsilon^{(m)}(x_{i+1/2}, \mu) - \mu \delta \epsilon^{(m)}(x_{i+1/2} - \alpha, \mu) + \int_{x_{i+1/2}-\alpha}^{0} \hat{\sigma}_t \delta \epsilon^{(m)} \mathrm{d}x \right) = \lim_{\alpha \to 0} r_{\text{face}}(x_{i+1/2}^-)$$
(77)

The integral goes to zero because $\delta \epsilon^{(m)}$ is smooth on the interior of the cell, and $\mu \delta \epsilon^{(m)}(x_{i+1/2} - \alpha, \mu)$ goes to zero because there is no source upstream of $x_{i+1/2}^-$. Thus, the final solution is

$$\delta \epsilon^{(m)}(x_{i+1/2}, \mu) = \frac{r_{\text{face}}(x_{i+1/2}^-)}{\mu} = \tilde{I}^{(m)}(x_{i+1/2}^-, \mu) - \tilde{I}^{(m)}(x_{i+1/2}, \mu). \quad (78)$$

The update for $I(x_{i+1/2}, \mu)$ is

$$\tilde{I}^{(m+1)}(x_{i+1/2}, \mu) = \tilde{I}^{(m)}(x_{i+1/2}, \mu) + \epsilon^{(m)}(x_{i+1/2}, \mu) + \delta \epsilon^{(m)}(x_{i+1/2}, \mu) \quad (79)$$
$$= \tilde{I}^{(m)}(x_{i+1/2}^-, \mu) + \epsilon^{(m)}(x_{i+1/2}, \mu). \quad (80)$$

This result has the peculiar effect that the estimation of the solution on a face depends only on the interior solution $\tilde{I}^{(m)}(x_{i+1/2}^-, \mu)$ and not the previous face value $\tilde{I}^{(m)}(x_{i+1/2}, \mu)$. This could be used to only estimate face values in particular cells, at any chosen batch.

0.16 Implementation of ECMC finite-element space, tallies, and residual sampling

The ECMC solver uses a finite element representation in space and angle. On the interior of the cell with the i-th spatial index and j-th angular index, the linear representation is defined as

$$\tilde{I}(x,\mu) = I_{a,ij} + \frac{2}{h_x}I_{x,ij}(x - x_i) + \frac{2}{h_\mu}I_{\mu,ij}(\mu - \mu_j), \quad x_{i-1/2} < x < x_{i+1/2}, \quad \mu_{j-1/2} \leq \mu \leq \mu_{j+1/2}$$

The spatial cell width is h_x, the angular width is h_μ, the center of the cell is (x_i, μ_j), and

$$I_{a,ij} = \frac{1}{h_x h_\mu} \iint_{\mathcal{D}} I(x,\mu)\,\mathrm{d}x\mathrm{d}\mu \tag{81}$$

$$I_{x,ij} = \frac{6}{h_x h_\mu} \iint_{\mathcal{D}} \left(\frac{x - x_i}{h_x}\right) I(x,\mu)\,\mathrm{d}x\mathrm{d}\mu \tag{82}$$

$$I_{\mu,ij} = \frac{6}{h_x h_\mu} \iint_{\mathcal{D}} \left(\frac{\mu - \mu_j}{h_\mu}\right) I(x,\mu)\,\mathrm{d}x\mathrm{d}\mu, \tag{83}$$

where $\mathcal{D} : x_{i-1/2} \leq x \leq x_{i+1/2} \times \mu_{j-1/2} \leq \mu \leq \mu_{j+1/2}$. Standard upwinding in space is used to define $I(\mu)$ on incoming faces.

This representation can directly be plugged into Eq. (23) and evaluated to produce the residual source in the ECMC HO transport problem. The MC source $r^{(m)}(x,\mu)$ in Eq. (25) consists of both face and volumetric sources and can produce positive and negative weight particles. The distribution for sampling particle coordinates, in space and angle, is based on the L_1 norm over space and angle of the residual [?]. A particular cell volume or face is sampled, and then rejection sampling [?] is used to sample from the appropriate distribution on the face or interior of the space-angle cell. If the residual is negative at the sampled coordinates, the weight of the particle history is negative.

During a MC batch, moments of the error are tallied. The necessary moments of the error are defined analogously to Eq.'s (81)–(83). The tallies are evaluated by weighting the particle density with the appropriate basis function and integrating along the history path through the cell. For the cell

average, the n-th particle makes the contribution

$$\epsilon_{a,ij}^n = \frac{1}{h_x h_\mu} \int_{s_o^n}^{s_f^n} w^n(x,\mu) \mathrm{d}s, \tag{84}$$

where s_o^n and s_f^n are the beginning and end of the n-th particle track in the cell and $w(x,\mu)$ is the weight of the error particle in the MC simulation. Weight is attenuated exponentially, i.e., $w(x,\mu) \propto \exp(-\sigma_t |x/\mu|)$. Substitution of the exponential attenuation of the weight produces the result

$$\epsilon_{a,ij}^n = \frac{w(x_0,\mu)}{\sigma_t h_x h_\mu} \left(1 - e^{-\sigma_t s^n}\right). \tag{85}$$

Here, $w(x_0,\mu)$ is the particle weight at the start of the path and s^n is the length of the track. The contribution of a particle track to ϵ_x is given by

$$\epsilon_{x,ij}^n = \frac{w(x_0,\mu)}{h_x^2 h_\mu \sigma_t} \left[x_0 - x_f e^{-\sigma_t s^n} + \left(\frac{\mu}{\sigma_t} - x_i\right)\left(1 - e^{-\sigma_t s^n}\right), \right] \tag{86}$$

where x_0 and x_f are the beginning and ending x coordinates of the n-th path. The contribution to the first moment in μ is

$$\epsilon_{\mu,ij}^n = \frac{w(x_0,\mu)}{h_\mu^2 h_x \sigma_t} (\mu - \mu_j)\left(1 - e^{-\sigma_t s^n}\right), \tag{87}$$

where the particle x-direction cosine μ does not change because it is a pure-absorber simulation. Finally, the moments of the error are simply the average contribution of all particles.

0.17 Adaptive Mesh Refinement

This section describes the adaptive refinement strategy for the ECMC algorithm. Detailed equations for performing projections between meshes and computing the residual source on the refined meshes can be found in [?]. At the end of the ECMC batch, refinement is performed in space-angle cells based on a jump indicator. The jump indicator is the magnitude of the different between $I(x,\mu)$ in adjacent cells, averaged over each edge. The value of the largest jump, out of the four edges within a cell, is used as the indicator

for that cell. Based on this indicator, the 20% of cells with the largest jump are refined. Future work will explore simply using ϵ to indicate refinement, rather than the jump error. The refinement of a cell is chosen to be symmetric, with each space-angle cell divided into four equal-sized cells. The solution for $\tilde{I}^{n+1}(x, \mu)$ of the batch is projected onto the finer mesh for the next batch. Because the dimensionality of the sample space has increased, we increase the number of histories per batch s.t. the ratio of the number of histories to total cells is approximately constant for all meshes. At the end of the last HO solve in a time step, $\tilde{I}^{n+1}$ is projected back onto the original, coarsest mesh and stored as $\tilde{I}^n$ for the next time step.
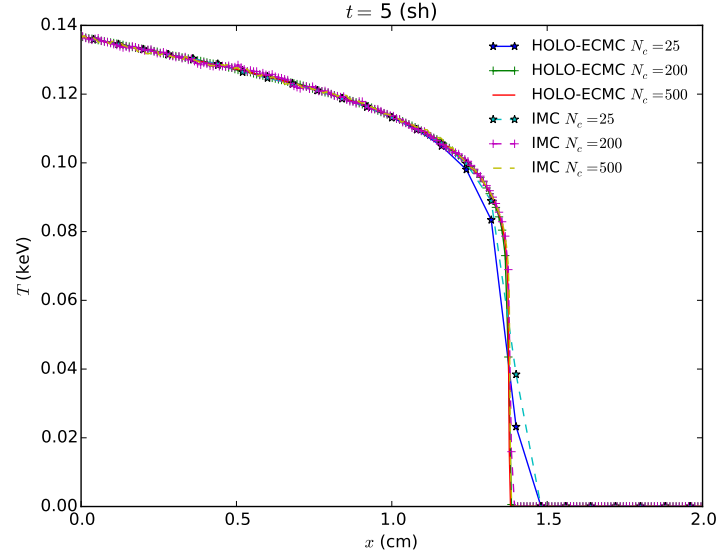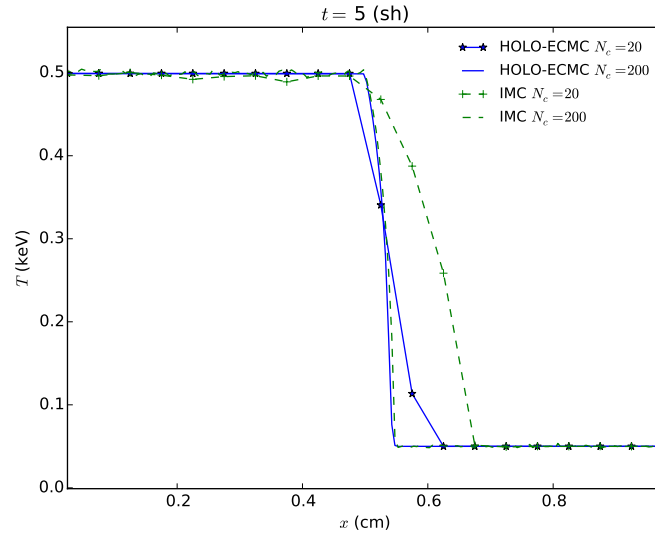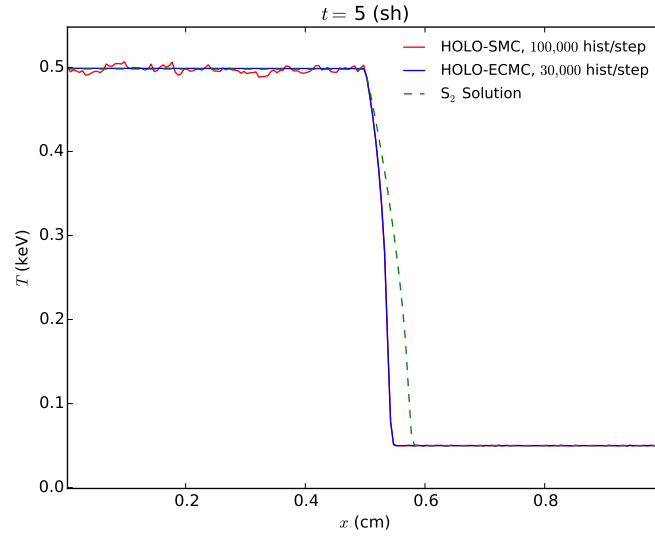
(a) Convergence of IMC and HOLO-ECMC solutions.
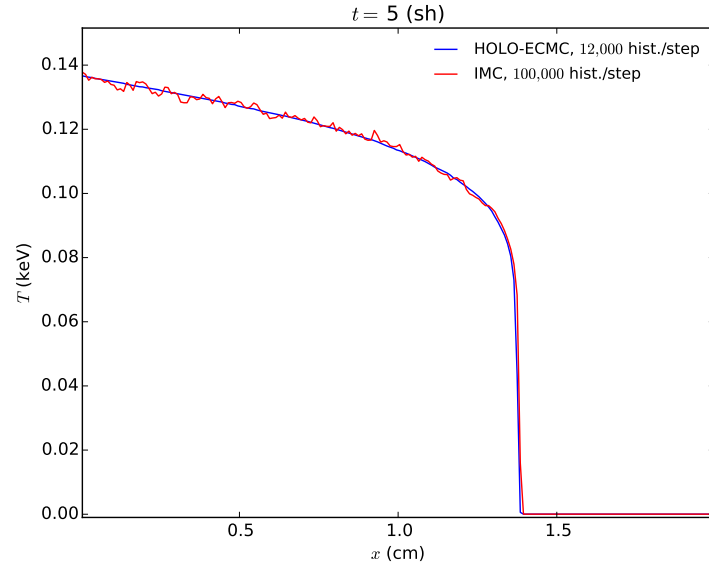
(b) Comparison of solutions for 200 spatial cells.

Figure 3: **Comparison of radiation temperatures for Marshak wave problem at t = 5 sh.**

(a) Comparison of IMC and HOLO-ECMC.

(b) Comparison of SMC and ECMC HO solvers.

Figure 4: **Comparison of radiation temperatures for two material problem.**
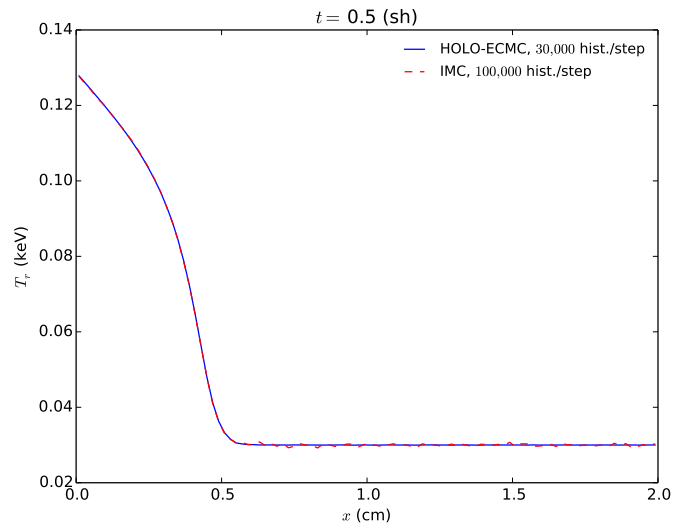
Figure 5: **Comparison of radiation temperatures for the pre-heated Marshak wave problem for 100 x cells at t = 0.5 sh.**